Faraday Discussions

Accepted Manuscript

Published on 01 July 2026

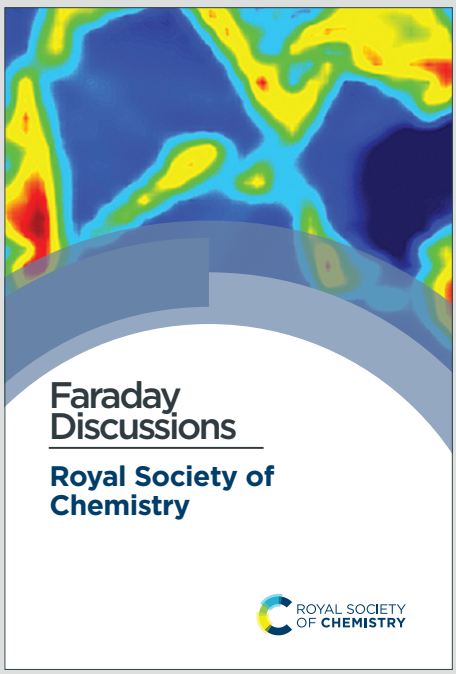

ROYAL SOCIETY OF CHEMISTRY

www.rsc.org/faraday_d

Faraday Discussions

PAPER

Investigating Halogen-Bond-Mediated Through-Space Activation of CO_2 for Electrocatalytic Reduction by Iron Porphyrins

Cecilia Albanese,[a,d] Sihem Groni,[b,d] Lauriane Chevalier,[d] Gabriele Di Carlo,[a] Francesca Tessore,*[a] Marc Robert,[b,d,e] Bernd Schöllhorn,[c] Niklas von Wolff,*[b] and Claire Fave*[b,d]

Received 00th January 20xx, Accepted 00th January 20xx
DOI: 10.1039/x0xx00000x

Developing novel molecular catalysts for electrochemical CO_2 reduction can play an important role for the development of highly selective transformations towards valuable compounds such as CO, HCOOH and CH_3OH. Iron porphyrins have shown promising activity in CO_2-to-CO electroreduction, as the porphyrin macrocycle structure can be modulated finely to tune CO_2 activation. Both charged and hydrogen-bonding substitutents on the porphyrin macrocycle were previously shown to enhance catalytic reduction. In the current study, we probe if halogen bonding (XB) could be leveraged as a new mode of CO_2 activation in iron porphyrin electrochemistry. A range of *ortho*-substituted iodo- and bromo iron porphyrins were synthesized and their electrochemical behaviour analyzed in detail. While all iodo-compounds and one bromo-compound lead to C-halogen bond cleavage at the potentials necessary for CO_2 reduction, all other bromo-complexes were shown to be highly selective for CO_2-to-CO electroreduction. Cyclic voltammetry and DFT calculations, combined with a detailed mechanistic analysis enabled to deconvolute through-bond and through-space effects in these novel XB-capable iron porphyrins and finds that σ-hole modulation mitigates unfavourable through-space repulsion at the reduced Fe(0) state.

Introduction

Environmental issues related to the increasing levels of CO_2 are a global challenge. Among various approaches, the electrochemical reduction of CO_2 into valuable compounds such as CO, HCOOH, CH_3OH, upon using electricity generated from renewable sources, is a promising and potentially green way to obtain industrial products, and to contribute to the development of a circular global economy. Due to significant kinetic barriers, the reduction of this gas requires the use of a catalyst that should promote selectively CO_2conversion into the desired products.[1–4]

In this context iron porphyrins have been shown to be selective molecular catalysts for the reduction of CO_2-to-CO.[5–7] Thanks to ligand tunability, porphyrins have a wide range of applications in diverse fields, such as sensing,[8] optoelectronics,[9] third generation photovoltaics[10] and artificial photosynthesis.[11,12] A judicious tailoring of the porphyrin macrocycle structure allows a modulation of its electronic properties, its solubility in various solvents and its redox potentials. In the past years, many studies have additionally pointed out the role of substituents on the ligand core in favouring the interaction between CO_2 and the iron at the centre of the macrocycle for boosting the CO_2-to-CO catalysis. Notably, the important role of moieties that can establish hydrogen bond or coulombic interactions (electric field effect) has been demonstrated, especially when situated in the 'ortho-ortho' position of the porphyrins' meso-phenyl rings, giving rise to "through-space interactions" with stabilization of the catalyst- CO_2 complex.[13,14] At the same time, the remarkable effect of such through-space interactions, well-described under homogeneous conditions, does not always translate into the most performing systems under heterogenous conditions in state-of-the-art gas diffusion electrode CO_2 electrolyzers. As an example, both *ortho*- and *para*-substituted cationic trimethyl ammonium tetraphenyl iron porphyrins show excellent catalytic activity for CO_2 to CO electroreduction.[13] Nevertheless, they remain less active than for example neutral cobalt phthalocyanine catalysts, once immobilized on carbon support in CO_2-electrolyzers.[15–17] Possible explanations might include that the charged environment, effective in activating CO_2 through electrostatic effects, could also lead to enhanced leaching of the molecular catalyst into the (aqueous) electrolyte or interfere with more advantageous cation activation of CO_2 through electrostatic repulsion.[18] In an effort to explore novel non-charged activation modes of CO_2 in molecular electrocatalysts, we here investigate the role of halogen bonding (XB) as a through-space interaction for the catalytic reduction of CO_2 with iron porphyrin catalysts. XB can be defined, according to the IUPAC, as a net attractive interaction between an electrophilic region associated with a halogen atom in a molecular entity and a nucleophile.[19] During the past three decades, XB has been reported for a wide range of applications, such as crystal engineering,[20–23] molecular recognition[24–28] and catalysis.[29–31] It has been shown that the electrochemical activation of either redox active XB donors or acceptors can promote the formation of stronger XB complexes.[32–35] Recently, several groups have reported using XB donors as co-catalysts in the conversion of CO_2 and epoxides into cyclic carbonates under thermal conditions.[36–39] This illustrates the relevance of employing non-covalent interactions in CO_2 transformation. Earlier this year, the first example of redox switchable XB-bonding for electrocatalysis was reported by Shida and

co-workers.[40] At the same time, XB has also been proposed to facilitate photochemical CO_2 reduction.[41,42] These precedents thus raise questions whether XB could also be exploited for electrocatalytic CO_2 reduction in non-charged molecular catalysts. To this end, we report here several halogenated iron porphyrins to explore the potential of XB activation of CO_2 under electrochemical conditions.[43]

Results and Discussion

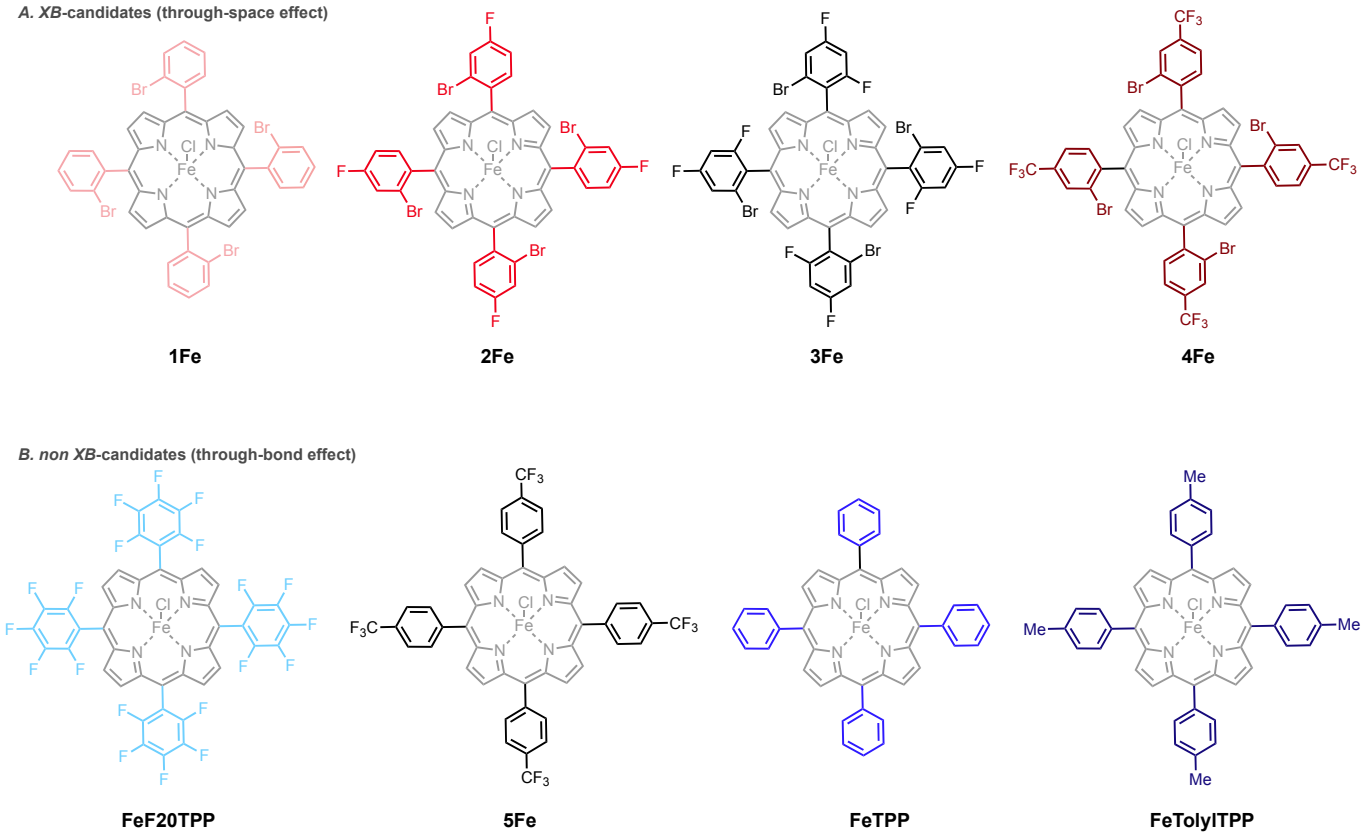

Scheme 1: Range of meso tetraphenyl iron porphyrins with *ortho*-bromine substituents on the phenyl rings, which could act as XB-donors (A). Range of meso tetraphenyl iron porphyrins of different electronic demand, that should rely exclusively on inductive "through-bond" effects (B). Both **3Fe** and **5Fe** show complicated electrochemical behaviour and have thus not been included in the quantitative kinetic analysis.

Both iodo- and bromo-substituted (*ortho*-position) iron porphyrins were selected, as their high polarizability (especially for iodinated compounds) can lead to particularly strong XB donor properties (see Scheme 1 and SI for synthetic details). Preliminary electrochemical studies on iodinated iron porphyrin derivatives however showed reduction potentials related to Fe(I)/Fe(0) processes very close to those of the dissociative C-I bond cleavage, as typically observed in iodo-arenes (Figure S1), rendering the iodo-derivatives incompatible with the envisioned redox-catalysis. We thus focused on *ortho*-brominated tetraphenyl porphyrin structures (Scheme 1), which are more stable within the activity window of iron porphyrins. Complementary electro-withdrawing groups (F, CF_3) have been introduced in order to increase the sigma hole on the halogen atom[44] and thus to modulate the strength of XB to probe potential effects on CO_2 activation. The ortho-brominated compounds **1Fe**, **2Fe**, **3Fe** and **4Fe**, were thus synthesized (see SI section 2), as well as a non-brominated compound **5Fe** (*para*-CF_3, but no *ortho*-Br) to serve as non-XB capable control.

Electrochemistry

We started our analysis by probing the electrochemical properties of the five porphyrins **1Fe** to **5Fe** by cyclic voltammetry (CV) and we compared them with 5,10,15,20-Tetraphenyl-21H,23H-porphine iron(III) chloride (**FeTPP**), considered as a benchmark catalyst for CO_2 reduction. The measurements were conducted under argon and CO_2 atmosphere, in an anhydrous DMF solution with 0.1 M of $TBAPF_6$, using a glassy carbon working electrode, a Pt-counter electrode and a Saturated Calomel Electrode (SCE) as reference electrode (T = 293 K). In the case of **3Fe** the irreversible cleavage of the four bromine substituents on the phenyl rings occurs at less negative potentials than the generation of the necessary active "Fe(0)" species (see SI, Figure S2-3). For this reason, this compound could not be used as a redox mediator for the catalytic CO_2 reduction and was not further analysed. The XB capable iron porphyrin **1Fe**, **2Fe** and **4Fe** all show three cathodic waves that can be ascribed to the three sequential formal one electron reductions to the formal oxidation states Fe(III)/Fe(II), Fe(II)/Fe(I) and Fe(I)/Fe(0). Moving towards more negative potentials, porphyrins **1Fe** and **2Fe** (see SI, Figure S6) displayed an additional wave at ca. –2.02 V vs SCE which was attributed to the cleavage of the C-Br bonds in the *ortho* position of the phenyl-rings (Figure S6). For **4Fe**, an additional a new reduction wave appeared at

more negative potentials (–2.40 V vs SCE), assigned to CF_3 cleavage. The electrochemical characteristics of all porphyrins in DMF solution are summarized in (Table 1). As expected, the standard reduction potentials shift towards less negative potentials upon the introduction of the electron withdrawing substituent CF_3 on the phenyl ring (e.g. $E^0_{Fe(III)/Fe(II)}$ (**1Fe**) = –0.13 V vs $E^0_{Fe(III)/Fe(II)}$ (**4Fe**) = –0.07 V vs SCE, Figure 1, left). Importantly, the third reduction wave, which generates the Fe(0) catalytically competent species, is shifted anodically by 150 mV with **4Fe**, as compared to **FeTPP**. In the absence of the CF_3 group on the phenyl rings (**1Fe**, **2Fe**) there is barely any differences compared to the **FeTPP** standard redox potential. When the CVs of porphyrins **1Fe**, **2Fe** and **4Fe** were recorded under CO_2 atmosphere (Figure 1, right), the two reduction waves corresponding to the formal Fe(III)/Fe(II) and Fe(II)/Fe(I) redox couples were only marginally modified. At the redox potential of the third reduction assigned to the Fe(I)/Fe(0) couple, a catalytic wave occurred in all cases (Figure 1, right).

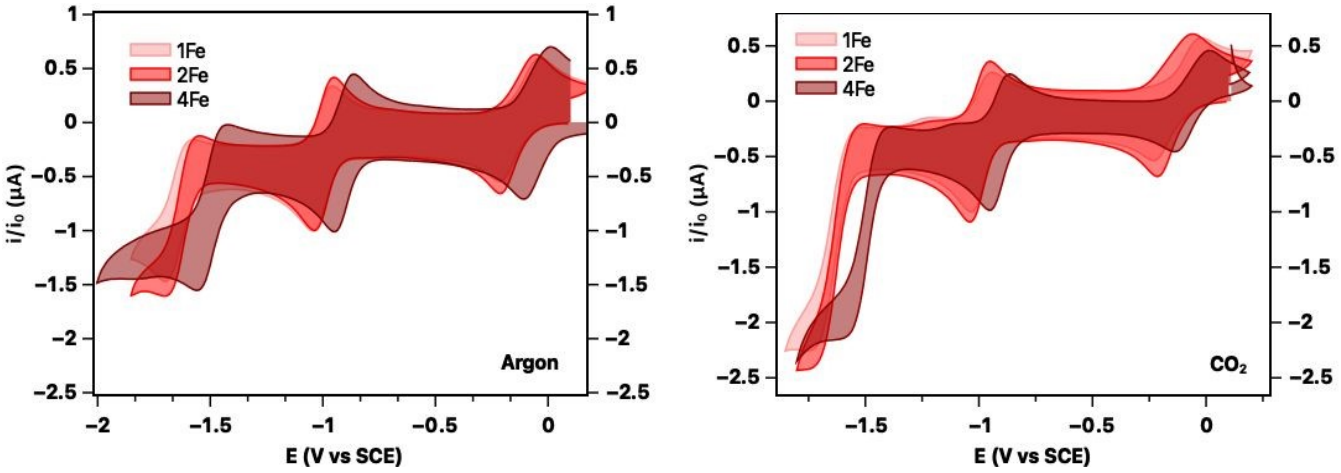

Figure 1: CVs for various Fe(III) porphyrins (0.5 mM) in DMF + 0.1 M TBAPF6 showing the three successive reduction waves, ν = 100 mV.s-1, under Argon (left) and under 1 atm CO2 (on the right). Currents have been normalized with respect to the Fe(II)/Fe(I) wave.

This behaviour corresponds to the interaction of CO_2 with the electrochemical generated Fe(0) species, leading to its catalytic reduction. The reduction potential of the catalytic wave strongly depends on the presence and the strength of electron-withdrawing groups. Fluorine and bromine atoms have only a minor effect on the decrease of the cathodic potentials of **1Fe** and **2Fe** compared with those of unsubstituted **FeTPP** (E^{cat}_{FeTPP} = –1.80 V *vs* $E^{cat}_{\mathbf{2Fe}}$ = –1.70 V). The catalytic wave on the Fe(I)/Fe(0) wave of **4Fe** bearing four CF_3 moieties occurred at the most positive potentials, - 1.60 V vs SCE, probably due to strong and determining electron-withdrawing effect of the para CF_3 substituents. Comparing the catalytic activity of **1Fe** and **2Fe**, a slight increase in catalytic current can be observed for the more electron-withdrawing fluorinated **2Fe**. The CF_3 substituted **4Fe** shows a similar catalytic activity as **1Fe**, but at more positive potentials (*i.e.* at lower overpotential). At first sight, these observations could align with a non-covalent (through-space) XB interactions of the polarized bromides with coordinated CO_2 at the formal Fe(0) oxidations state, promoting its catalytic reduction. Increasing the sigma hole on the bromine atoms by increasing the electron-withdrawing character moving from **1Fe** to **2Fe** and **4Fe** would thus lead to enhanced activation of an intermediate Fe(0)-CO_2 adduct, that is then catalytically reduced.

Table 1: Electrochemical apparent standard redox potentials (in V *vs* SCE) for the different iron porphyrins under investigation in DMF, 0.1 M $TBAPF_6$.

Property/Compound	1Fe	2Fe	4Fe	5Fe	FeF20TPP	FeTPP	FeTolylTPP
$E^{0'}_{Fe(III)/Fe(II)}$	–0.13	–0.13	–0.07	–0.09	–0.01	–0.13	–0.16
$E^{0'}_{Fe(II)/Fe(I)}$	–0.99	–0.99	–0.91	–0.94	–0.83	–1.01	–1.03
$E^{0'}_{Fe(I)/Fe(0)}$	–1.63	–1.62	–1.49	–1.49	–1.37	–1.65	–1.67

In order to analyze this potential XB-effect in more detail, it is necessary to obtain quantitative kinetic information on the respective catalytic processes. While in general catalytic plateau currents can provide straightforward kinetic information for a known underlying mechanism,[45] the situation in the case of **1Fe**, **2Fe** and **4Fe** is more complicated due to the presence of side-phenomena at reductive potentials, such as the cleavage of C-Br and the CF_3-groups (see SI, Figure S6). In order to have a more quantitative analysis of potential XB effects, catalytic rate constants (k_{cat}) were thus calculated by the foot-of-the-wave approach (FOTWA),[46] both in the absence and in the presence of increasing concentrations of a suitable proton donor (PhOH, see Table 2 and SI, section 5 for details). In order to rule out secondary effects on the observed catalytic activity due to competitive reaction pathways (e.g. hydrogen evolution), controlled potential electrolysis was performed, confirming highly selective CO production and the absence of H_2 formation in all cases (see SI section 4, Table S1). At 1M PhOH, an increase of the rate constant moving from **1Fe** (258.9 ± 16.2 s^{-1} M^{-1}) to **2Fe** (287.7 ± 4.9 s^{-1} M^{-1}) was observed, despite the more electron-withdrawing character of the fluorine atoms in **2Fe**, potentially indicative of a XB-activation of CO_2. Moving to **4Fe**, the rate constant drops to 144.7 ± 0.3 s^{-1} M^{-1}, which is line with the much less negative reduction potential of the Fe(I)/Fe(0) wave in **4Fe**, making the Fe(0) active catalyst less nucleophilic towards

CO_2 in this latter case.[46] Clearly, any possible (positive) XB-effect on the rate constant would thus be convoluted with (negative) inductive "through-bond" effects, when trying to compare **1Fe** and **2Fe** to **4Fe**.

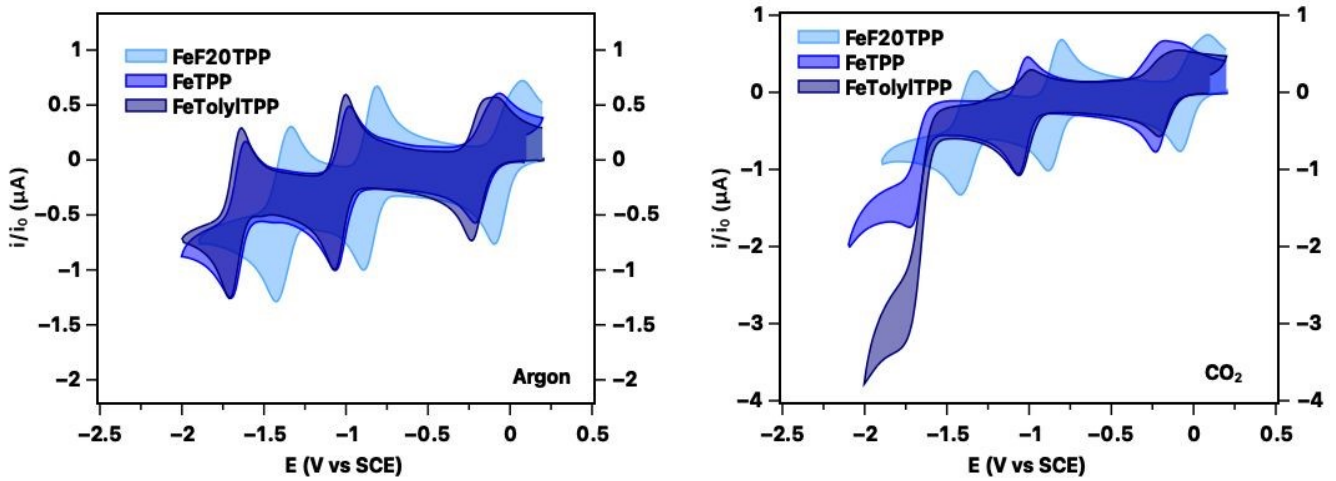

Figure 2: CVs for various "through-bond" effect Fe(III) porphyrins (0.5 mM) in DMF + 0.1 M $TBAPF_6$ showing the three successive reduction waves, ν = 100 $mV.s^{-1}$, under Argon (left) and under 1 atm CO_2 (on the right). Currents have been normalized with respect to the Fe(II)/Fe(I) wave.

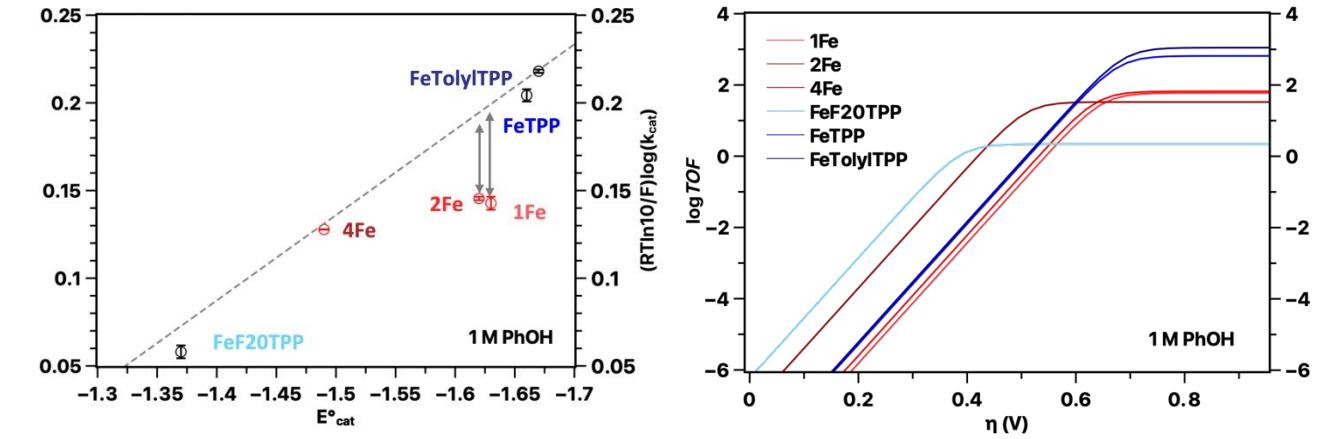

Figure 3: Correlation between the catalytic rate constant and the catalyst standard potential (V *vs* SCE) at 1M PhOH concentration (Left). Gray arrows indicate deviation from ideal (through-bond) correlation. Comparative catalytic Tafel plots for the three XB-candidate catalysts (**1Fe**, **2Fe** and **4Fe**), as well as for three "through-bond" catalysts (**FeF20TPP, FeTPP** and **FeTolylTPP**) at 1M PhOH concentration (Right).

As shown for the earlier-mentioned charged trimethyl ammonium iron porphyrins, electrostatic through-space effects can be quantified by comparison to the catalytic activity of pure through-bond activated benchmark catalysts.[13] Indeed, a linear correlation of the reduction potential of the Fe(I)/Fe(0) wave ($E°_{cat}$) with the logarithm of the rate constant is expected in the absence of through-space effects[46] and on the contrary, species capable of through-space CO_2 activation would be expected outside this linear correlation regime. As benchmarks, we thus also probed the CO_2 reduction activity of **FeTPP**, its *para*-methylated version **FeTolylTPP**, the perfluorinated **FeF20TPP**, as well as the *para*-CF_3 substituted **5Fe** (Figure 2, left). In the absence of phenol, the most electron-withdrawing **FeF20TPP** shows barely any enhancement of catalytic activity (Figure 2, right). The two more electron-donating **FeTPP** and **FeTolylTPP** on the other hand, show strong current enhancement under CO_2 atmosphere (Figure 2, right). Similarly, also **5Fe** shows catalytic activity under CO_2 but no access to reliable kinetic information was possible due to electrochemical events close to the Fe(I)/Fe(0) wave (see SI, Figure S4-S5), for which reason it was excluded from further analysis. At 1M PhOH, all four through-bond complexes show catalytic activity, although no clear plateau-shaped currents were observable (see SI, Figure S7-S9). Again, FOTWA-analysis allowed to access kinetic constants under these conditions. Increasing the electron-donating character from **FeF20TPP** to **FeTPP** and **FeTolylTPP** increased the rate constant from 9.6± 0.6 to 2839.6 ± 167.6 and 4847.7 ± 76.7 s^{-1} M^{-1} (Table 2). Having access to quantitative kinetic data of these "pure inductive" iron porphyrins, then allows to deconvolute through-space effects in **1Fe**, **2Fe** and **4Fe** by comparison.

As expected, **FeF20TPP, FeTPP** and **FeTolylTPP** follow the expected linear correlation of the standard potential of the Fe(I)Fe(0) wave ($E_{cat}°$) with log(k_{cat}) (see Figure 3). The potentially XB-capable porphyrins **1Fe** and **2Fe** (**4Fe** to a lesser extend) on the other hand fall outside this linear regime, indicative of distinct through-space effects (Figure 3, left). These effects are, however, destabilizing in nature as both **1Fe** and **2Fe** fall below the expected (as of $E_{cat}°$) value of k_{cat} (see grey arrows, Figure 3). At the same

time, this destabilizing effect seems to be attenuated (*i.e.* less deviation from the linear trend) with increasing electron-withdrawing character of the *para*-substituents on the porphyrins (H *vs* F *vs* CF_3).

Table 2: Kinetic rate constants and sigma-hole strength (where applicable) for the different compounds under investigation.

Property/Compound	1Fe	2Fe	4Fe	FeF20TPP	FeTPP	FeTolylTPP
k_{cat} (s^{-1} M^{-1})	258.9 ± 16.2	287.7 ± 4.9	144.7 ± 0.3	9.6± 0.6	2839.6 ± 167.6	4847.7 ± 76.7
V_σ (a.u.)	–0.1479	–0.1381	–0.1313	n.a.	n.a.	n.a.
$V_\sigma^{free-base}$ (a.u.)	+0.0034	+0.0133	+0.0209	n.a.	n.a.	n.a.
dV_σ (a.u.)	+0.0222	+0.0245	+0.0171	n.a.	n.a.	n.a.

DFT calculations

To understand these observations in more detail and to verify if these trends are in line with possible XB-bond activation of CO_2, we performed additional DFT calculations (see SI, section 6 for details). The halogen bond donor abilities of the bromo-porphyrin derivatives can be estimated from the calculation of their respective Electrostatic Surface Potential (ESP) and more precisely from its magnitude at the site of the σ-hole (Figure 4). In the free-base porphyrins, the σ-hole size (V_σ) increases in the order from **1** < **2** < **4** in agreement with the increased electron-withdrawing character of the substituents H < F < CF_3 (0.0034, 0.0133 and 0.0209 a.u., respectively, Table 2).[47] This increase in sigma-hole strength is thus seemingly in agreement with the enhanced activity of **2Fe** compared to **1Fe** and the similar activity of **4Fe** despite its much less negative E_{cat}°. While as mentioned above some reports exist on XB-bonding for the photoreduction of CO_2,[41,42] it is unclear if sigma-hole strength remains also at the redox potential E_{cat}° necessary for catalytic turnover under electrochemical conditions. At this potential, *i.e.* at the respective formal Fe(0) stage, the complexes bear an overall charge of –2, which could strongly limit sigma-hole strength.

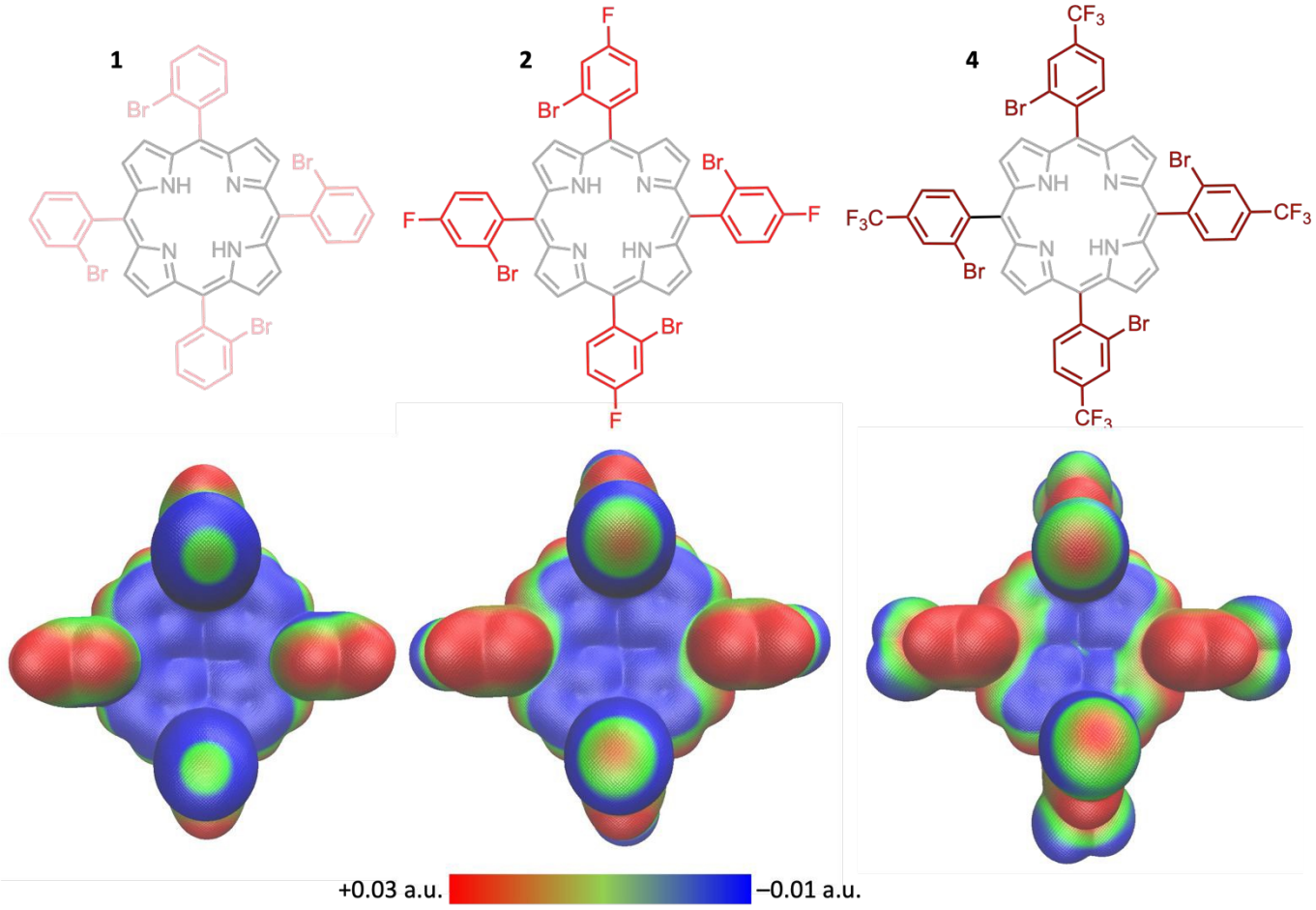

Figure 4: Top view of ESP surface charges at the 0.001 isosurface value for the free-base porphyrins **1**, **2** and **4**. Sigma-holes on the bromines are visible.

We thus also computed the sigma-hole strength of the iron porphyrins **1Fe**, **2Fe** and **4Fe** at the formal Fe(0) oxidation state (overall charge of –2). Again, an increase of sigma-hole strength is observed moving from H and F to the CF_3 substituent (**1Fe** < **2Fe** < **4Fe**), but the overall value of the "sigma-hole" remains negative for all complexes (–0.1479, –0.1381 and –0.1313 a.u., respectively, Figure 5, Table 2). While these "sigma-holes" indeed show comparatively positive charge built-up with respect to their surrounding (ESP differences dV_σ between +0.0171 and +0.0245 a.u. was computed for **1Fe**, **2Fe** and **4Fe** at the Fe(0) level, Table 2), the overall

negative charge at the sigma-hole raises questions about the positive influence on CO_2 activation. Again, at the formal Fe(0) state, we computed potential CO_2-adducts of **1Fe**, **2Fe** and **4Fe**. As shown in Figure 6, all complexes remain nucleophilic enough to form stable CO_2-adducts. However, for both **1Fe** and **2Fe**, the CO_2 moiety moves away from the adjacent C-Br bonds during optimization, demonstrative of repulsive interactions between the partially negatively charged oxygen atoms in the CO_2-adduct and the negative charge of the sigma-hole on the bromine atoms (see also Table 2). In **4Fe**, the CO_2-adduct remains in the direction of the C-Br bonds, in line with a less negative value of the sigma-hole (–0.1313 a.u.), but a slight twist of the phenyl rings is nevertheless observed, thus repulsion between the sigma-hole and the CO_2 fragment remains.

Discussion

These calculations now allow to draw a clearer picture of the effect of XB-bonding on CO_2 activation and to rationalize the observed rate constants for electrochemical CO_2 reduction. From Figure 6 and our DFT calculations it becomes clear that the role of increasing the sigma-hole strength from **1Fe** to **2Fe** and **4Fe** is to reduce the electrostatic repulsion between the *ortho*-Br substituents and the Fe-CO_2 adduct. Similar unfavourable through-space interactions have been observed for other anionic iron porphyrins (e.g. *para*-tetrasulfonato-FeTPP),[13] characterized by a deviation from the linear $E°_{cat}$ *vs* log(k_{cat}) correlation. Increasing the sigma-hole thus leads to a less marked deviation from expected catalytic activity (vertical lines in Figure 3) so that for **4Fe** the repulsive through-space effect is almost cancelled. Another way of understanding through-space *vs* through-bond activation is by looking at catalytic Tafel plots.[46,48] A catalytic Tafel plot correlates the turnover frequency (TOF) to the potential E or the overpotential η, with $\eta = E°_{CO_2/CO,DMF} - E$ ($E°_{CO_2/CO,DMF}$ = -0.74V vs SHE). The TOF is defined here as the ration of $N_{product}/N_{active\ cat}$ with $N_{product}$ equal the number of moles of product generated per unit of time and $N_{active\ cat}$ equal the maximal number of moles of active catalyst present in the reaction-diffusion layer only. It has been already reported that efficient catalysts are located on the top left of the Catalytic Tafel plot.

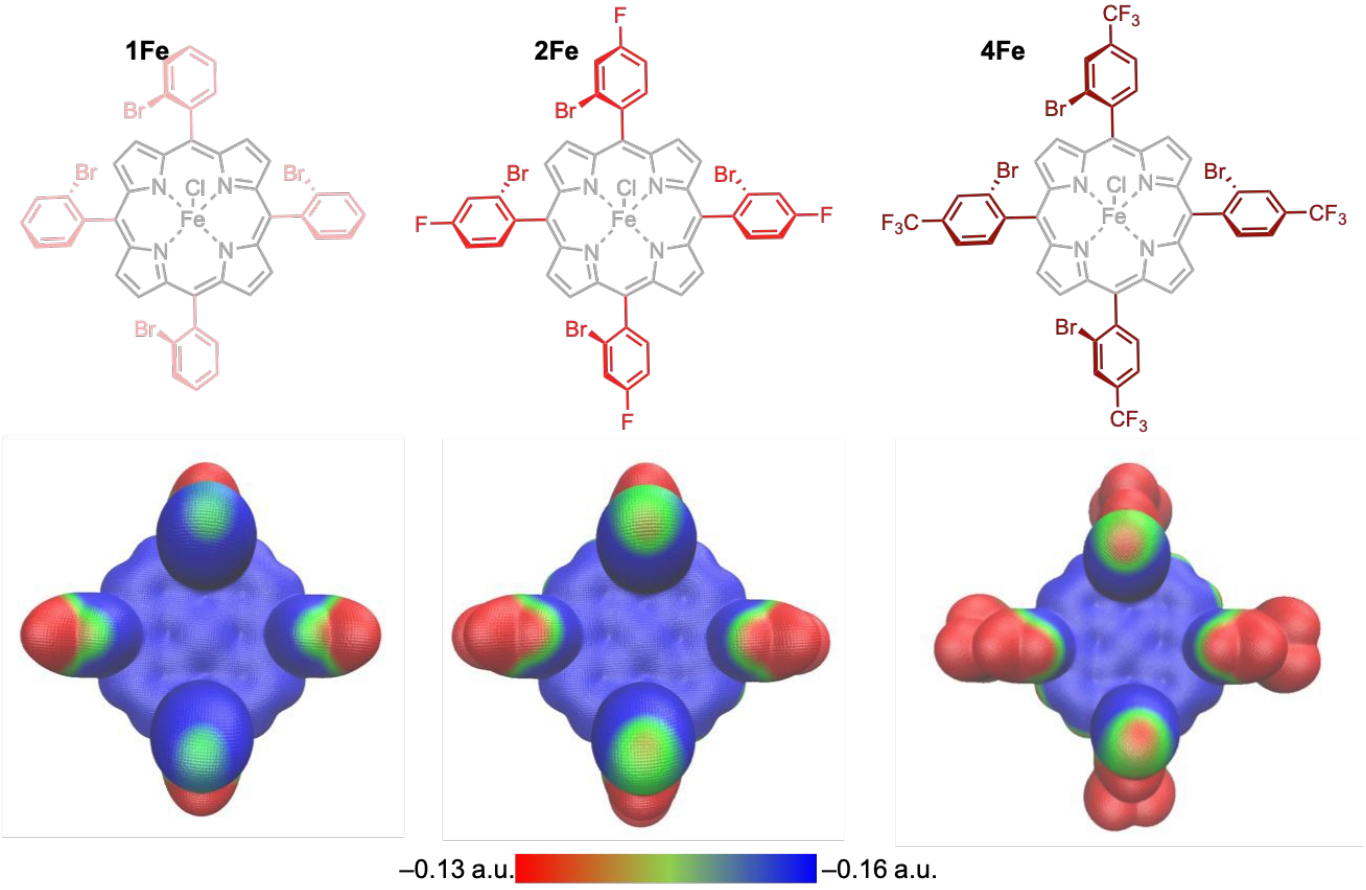

Figure 5: Top view of ESP surface charges at the 0.001 isosurface value for complexes **1Fe**, **2Fe** and **4Fe** at the formal Fe(0) state, *i.e.* at an overall charge of –2. Relatively positive "sigma-holes" are visible on the bromine atoms. Be aware of the different scale compared to Figure 4.

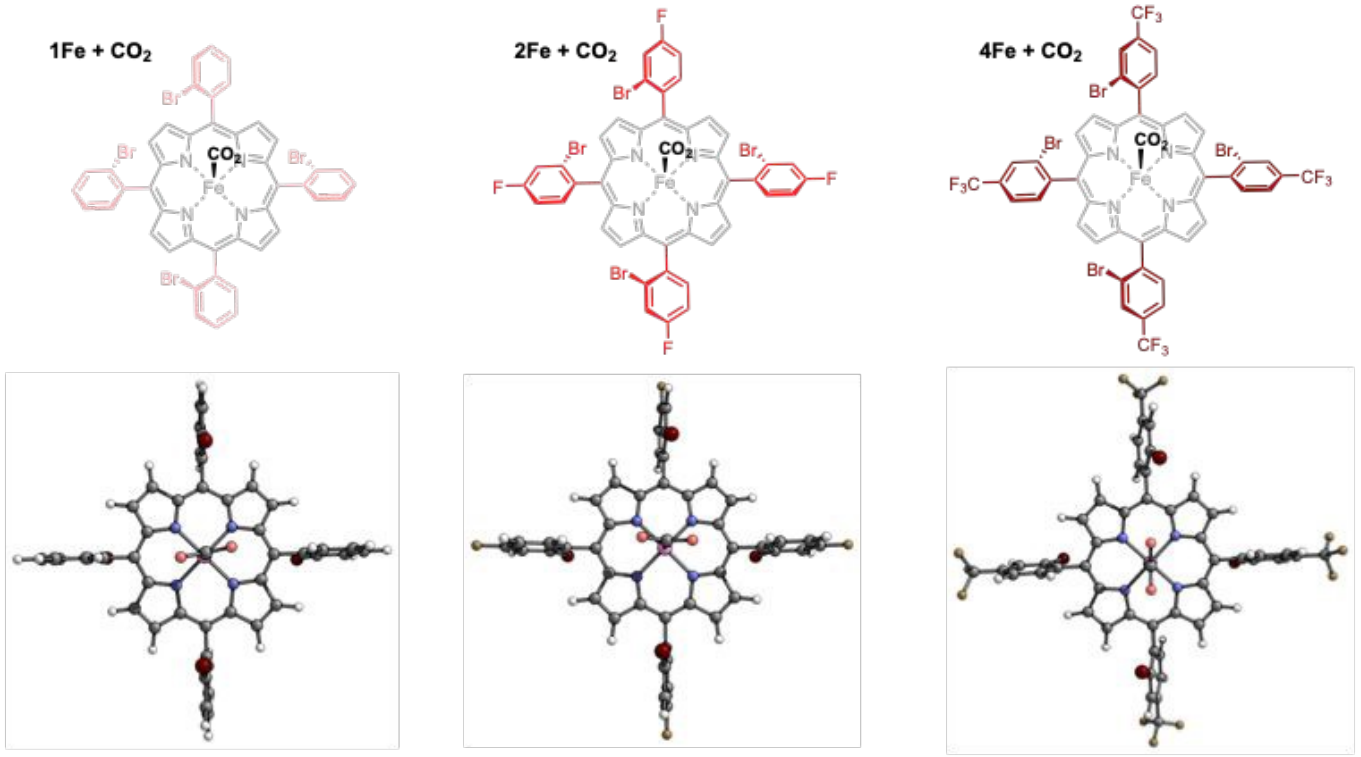

Figure 6: Computed CO_2 adducts of the complexes **1Fe**, **2Fe** and **4Fe** at the formal Fe(0) oxidation state. For both **1Fe** and **2Fe**, CO_2 is perpendicular to the C-Br axis. In **4Fe** a slight dihedral twist of the phenyl group is observed to diminish Br-CO_2 repulsion.

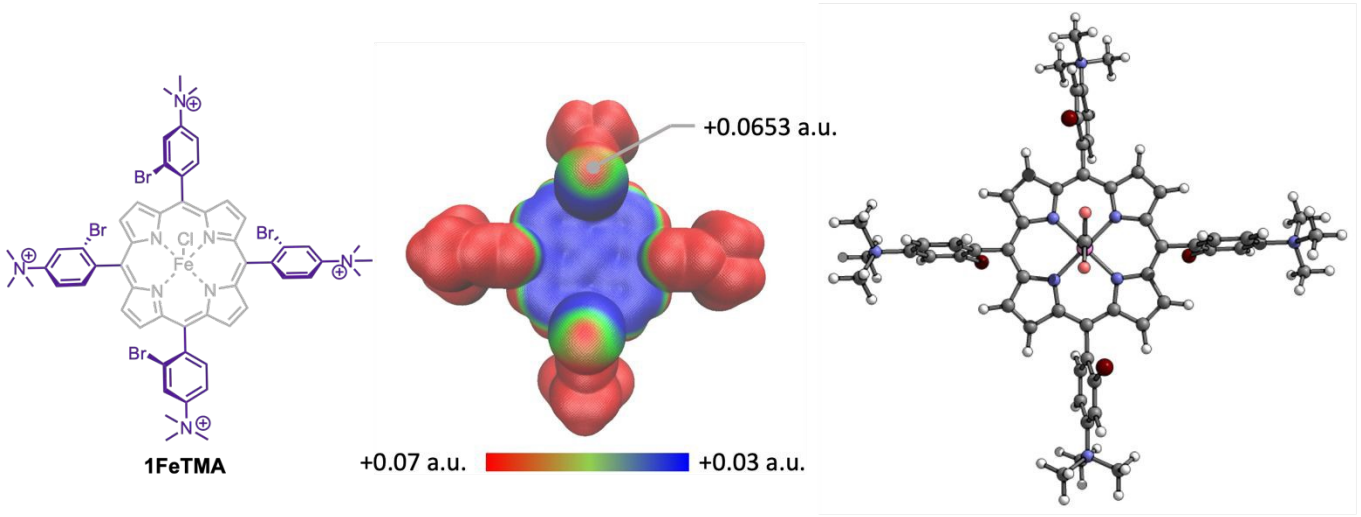

Scheme 2: Proposed structure of the *para*-trimethylammonium *ortho*-bromo tetraphenyl iron porphyrin **1FeTMA** (left), the ESP surface charge at the 0.001 electron density isosurface at the formal Fe(0) oxidation state (middle), as well as the optimized structure of the Fe-CO_2 at the formal Fe(0) oxidation state (right).

As can be seen in Figure 3 (right), both **1Fe** and **2Fe** show lower TOF values at similar overpotential η compared to **FeTPP** and **FeTolylTPP** having similar $E°_{cat}$, demonstrating that activating XB-bonding does not take place. In the case of **4Fe** significant TOF values can be achieved at low η, but the size/strength of the sigma-hole does not yet lead to a net beneficial effect (see also Figure 5). Given that for **4Fe** electrostatic repulsion is almost compensated, we were curious to understand if stronger sigma-holes could persist at the formal Fe(0) level in *ortho*-brominated tetraphenyl iron porphyrins. As an outlook for future catalyst design, we thus investigated by DFT the sigma-hole strength of a hypothetical *para*-trimethyl ammonium substituted *ortho*-bromo iron porphyrin (**1FeTMA**, Scheme 2). As the four trimethyl ammonium groups introduce positive charges, the complex will be charged +2 overall at the formal Fe(0) state. Calculating the ESP charge at the sigma-hole on the bromine atoms in **1FeTMA**, a value of +0.0653 a.u. indicates important positive charge built-up (higher than for all free-base porphyrins **1**, **2** and **4**) at the Fe(0) level. Despite the overall +2 charge, **1FeTMA** remains nucleophilic enough to stabilize a CO_2 adduct (Scheme 2). We are currently exploring if such compounds could pave the way towards high performing electrocatalysts operating *via* XB-activation of CO_2.

Conclusions

In conclusion, a range of potential XB-capable iron porphyrins were synthesized and their electrochemical behaviour was probed in detail. If designed carefully, reductive cleavage of the C-X substituent can be avoided. Such compounds can thus be employed as electrocatalysts for CO_2 reduction. The ortho-bromine substituted iron porphyrins that remain sufficiently stable under the catalytic potential window show high activity in CO_2 reduction with excellent faradaic efficiency towards CO. A detailed kinetic analysis using the foot-of-the-wave approach of potential XB-effect demonstrated that an increasing sigma hole indeed correlates with higher catalytic activity. DFT calculations revealed that the introduction of proper moieties capable of enhancing the sigma hole of the XB donor produces a through-space effect, mainly reducing the electrostatic repulsion with CO_2 rather than activating it through halogen bonding. We hope that this in-depth analysis will allow in the future to design new generation catalysts relying on through space effects that would allow to break inductive linear scaling relationships.

Author contributions

Conceptualization: B.S., C.F., M.R; investigation: C.A., S.G., L.C., N.v.W.; writing – original draft: C.F., N.v.W.; writing – review & editing: C.A., S.G., L.C., N.v.W., G.D.C., F.T., M.R., B.S., C.F.; data curation: C.A., N.v.W., C.F. formal analysis: N.v.W., C.F.; funding acquisition: M.R, C.F, F.T.; methodology: N.v.W., B.S., C.F., G.D.C., F.T.; supervision: N.v.W. B.S., C.F., M.R., G.D.C., F.T.
The manuscript was written through contributions of all authors. All authors have given approval to the final version of the manuscript.

Conflicts of interest

The authors have no conflicts of interest to declare.

Data availability

Synthesis and characterization of the iron porphyrins, experimental details on electrochemical experiments, methods for DFT calculations and ESP analysis, as well as for FOTWA are detailed in the Supporting Information. All electrochemical raw data and all data used to extract kinetic information can be obtained as *Origin* or *Qtiplot* project upon reasonable request from the authors. A data set collection of computational results is available in the ioChem-BD[49-50] repository and can be accessed via https://doi.org/10.19061/iochem-bd-6-666.

Acknowledgements

Partial financial support from ANR-18-IDEX-0001, Idex Université Paris 2019 is gratefully acknowledged.
Computations were performed using HPC resources from GENCI-CINES (Grant AD010812061R3 and Grant AD010812061R4).

[a.] *Department of Chemistry, University of Milano, INSTM RU, via Golgi 19, 20133 Milano, Italy.*
[b.] *Sorbonne Université, CNRS, Institut Parisien de Chimie Moléculaire, IPCM, Paris F-75005, France.*
[c.] *Université Paris Cité, ITODYS, F-75013 Paris, France.*
[d.] *Université Paris Cité, F-75013 Paris, France.*
[e.] *Institut Universitaire de France (IUF), F-75005, Paris, France.*

Notes and references

1 J.-M. Savéant, *Chem. Rev.*, 2008, **108**, 2348–2378.
2 J. Bonin, A. Maurin and M. Robert, *Coord. Chem. Rev.*, 2017, **334**, 184–198.
3 E. Boutin and M. Robert, *Trends Chem.*, 2021, **3**, 359–372.
4 C. Casadevall and J. Lloret-Fillol, in *Earth-Abundant Transition Metal Catalyzed Reactions*, Academic Press, 2024, vol. 74, pp. 181–256.
5 C. Costentin, M. Robert and J.-M. Savéant, *Acc. Chem. Res.*, 2015, **48**, 2996–3006.
6 R. Francke, B. Schille and M. Roemelt, *Chem. Rev.*, 2018, **118**, 4631–4701.
7 L. Sun, V. Reddu, A. C. Fisher and X. Wang, *Energy Environ. Sci.*, 2020, **13**, 374–403.
8 F. Tessore, E. Pargoletti, G. Di Carlo, C. Albanese, R. Soave, M. I. Trioni, F. Marelli and G. Cappelletti, *ACS Appl. Mater. Interfaces*, 2024, **16**, 41086–41098.

9 G. Di Carlo, M. Pizzotti, S. Righetto, A. Forni and F. Tessore, *Inorg. Chem.*, 2020, **59**, 7561–7570.
10 A. Covezzi, A. O. Biroli, F. Tessore, A. Forni, D. Marinotto, P. Biagini, G. D. Carlo and M. Pizzotti, *Chem. Commun.*, 2016, **52**, 12642–12645.
11 A. Orbelli Biroli, F. Tessore, G. Di Carlo, M. Pizzotti, E. Benazzi, F. Gentile, S. Berardi, C. A. Bignozzi, R. Argazzi, M. Natali, A. Sartorel and S. Caramori, *ACS Appl. Mater. Interfaces*, 2019, **11**, 32895–32908.
12 G. Di Carlo, C. Albanese, A. Molinari, S. Carli, R. Argazzi, A. Minguzzi, F. Tessore, E. Marchini and S. Caramori, *ACS Appl. Mater. Interfaces*, 2024, **16**, 14864–14882.
13 I. Azcarate, C. Costentin, M. Robert and J.-M. Savéant, *J. Am. Chem. Soc.*, 2016, **138**, 16639–16644.
14 C. Costentin, S. Drouet, M. Robert and J.-M. Savéant, *Science*, 2012, **338**, 90.
15 K. Torbensen, C. Han, B. Boudy, N. von Wolff, C. Bertail, W. Braun and M. Robert, *Chem. – Eur. J.*, 2020, **26**, 3034–3038.
16 C. Liu, D. Joulié, J. Shao, B. Giri, M. G. Gebru, U. Isci and M. Robert, *ACS Energy Lett.*, 2025, **10**, 4957–4961.
17 S. Ren, D. Joulié, D. Salvatore, K. Torbensen, M. Wang, M. Robert and C. P. Berlinguette, *Science*, 2019, **365**, 367.
18 Z. Zhang, H. Li, Y. Shao, L. Gan, F. Kang, W. Duan, H. A. Hansen and J. Li, *Nat. Commun.*, 2024, **15**, 612.
19 G. R. Desiraju, P. S. Ho, L. Kloo, A. C. Legon, R. Marquardt, P. Metrangolo, P. Politzer, G. Resnati and K. Rissanen, *Pure Appl. Chem.*, 2013, **85**, 1711–1713.
20 P. Metrangolo, F. Meyer, T. Pilati, G. Resnati and G. Terraneo, *Angew. Chem. Int. Ed.*, 2008, **47**, 6114–6127.
21 M. Fourmigué, *Curr. Opin. Solid State Mater. Sci.*, 2009, **13**, 36–45.
22 P. Metrangolo, G. Resnati, T. Pilati and S. Biella, in *Halogen Bonding: Fundamentals and Applications*, eds. P. Metrangolo and G. Resnati, Springer, Berlin, Heidelberg, 2008, pp. 105–136.
23 A. Mukherjee, S. Tothadi and G. R. Desiraju, *Acc. Chem. Res.*, 2014, **47**, 2514–2524.
24 C. Fave and B. Schöllhorn, *Curr. Opin. Electrochem.*, 2019, **15**, 89–96.
25 G. Cavallo, P. Metrangolo, T. Pilati, G. Resnati, M. Sansotera and G. Terraneo, *Chem. Soc. Rev.*, 2010, **39**, 3772–3783.
26 M. Erdélyi, *Chem. Soc. Rev.*, 2012, **41**, 3547–3557.
27 J. Pancholi and P. D. Beer, *Coord. Chem. Rev.*, 2020, **416**, 213281.
28 T. M. Beale, M. G. Chudzinski, M. G. Sarwar and M. S. Taylor, *Chem. Soc. Rev.*, 2013, **42**, 1667–1680.
29 R. L. Sutar and S. M. Huber, *ACS Catal.*, 2019, **9**, 9622–9639.
30 S. Benz, A. I. Poblador-Bahamonde, N. Low-Ders and S. Matile, *Angew. Chem. Int. Ed.*, 2018, **57**, 5408–5412.
31 M. Breugst and J. J. Koenig, *Eur. J. Org. Chem.*, 2020, **2020**, 5473–5487.
32 S. Groni, T. Maby-Raud, C. Fave, M. Branca and B. Schöllhorn, *Chem. Commun.*, 2014, **50**, 14616–14619.
33 J. Y. C. Lim, M. J. Cunningham, J. J. Davis and P. D. Beer, *Chem. Commun.*, 2015, **51**, 14640–14643.
34 H. Hijazi, A. Vacher, S. Groni, D. Lorcy, E. Levillain, C. Fave and B. Schöllhorn, *Chem. Commun.*, 2019, **55**, 1983–1986.
35 R. Oliveira, S. Groni, C. Fave, M. Branca, F. Mavré, D. Lorcy, M. Fourmigué and B. Schöllhorn, *Phys. Chem. Chem. Phys.*, 2016, **18**, 15867–15873.
36 K. Torita, R. Haraguchi, Y. Morita, S. Kemmochi, T. Komatsu and S. Fukuzawa, *Chem. Commun.*, 2020, **56**, 9715–9718.
37 K. Chen, R. Yan, Z. Li, W. Huang, L. Gao, T. Duan, H. Tong, Y. Li, J. Sun and K. Guo, *J. CO2 Util.*, 2021, **52**, 101663.
38 R. Yan, K. Chen, Z. Li, Y. Qu, L. Gao, H. Tong, Y. Li, J. Li, Y. Hu and K. Guo, *ChemSusChem*, 2021, **14**, 738–744.
39 S. Akbaba, M. Alvarez, S. Groni, B. Schöllhorn and C. Fave, *Tetrahedron Lett.*, 2023, **130**, 154760.
40 A. Hirama, K. Suda, S. Yoshinaga, M. Kikuchi, S.-G. Chong, A. Kikuchi, Y. Ishigaki, D. Yokogawa, M. Atobe and N. Shida, *J. Am. Chem. Soc.*, 2026, **148**, 6249–6257, 10.1021/jacs.5c1817.
41 X. Chen, C. Peng, W. Dan, L. Yu, Y. Wu and H. Fei, *Nat. Commun.*, 2022, **13**, 4592.
42 K. M. Batoo, E. Ali, B. A. Hussein, A. Al-khalidi, U. S. Altimari, S. Hussain, S. H. Kareem, M. K. Abid, A. Alawadi and A. Ihsan, *J. Mol. Struct.*, 2024, **1307**, 137927.
43 C. Albanese, *From Synthesis to Application: Porphyrins as Versatile Compounds in Energy, Sensing, and Catalysis*, Università degli studi di Milano, 2024.
44 G. Cavallo, P. Metrangolo, R. Milani, T. Pilati, A. Priimagi, G. Resnati and G. Terraneo, *Chem. Rev.*, 2016, **116**, 2478–2601.
45 C. Costentin and J.-M. Savéant, *ChemElectroChem*, 2014, **1**, 1226–1236.
46 I. Azcarate, C. Costentin, M. Robert and J.-M. Savéant, *J. Phys. Chem. C*, 2016, **120**, 28951–28960.
47 N. von Wolff, nvonwolff/Sigma-Hole-Analysis Zenodo 2026, https://doi.org/10.5281/zenodo.18541557.
48 C. Costentin, S. Drouet, M. Robert and J.-M. Savéant, *J. Am. Chem. Soc.*, 2012, **134**, 11235–11242.
49 M. Álvarez-Moreno, C. de Graaf, N. López, F. Maseras,J.M. Poblet, C.J. Bo, *Chem. Inf. Model.* 2015, **55**, 95–103.
50 C. Bo, F. Maseras, N. López, *Nat. Catal.* 2018, **1**, 809–810.

Data availability

Synthesis and characterization of the iron porphyrins, experimental details on electrochemical experiments, methods for DFT calculations and ESP analysis, as well as for FOTWA are detailed in the Supporting Information. All electrochemical raw data and all data used to extract kinetic information can be obtained as *Origin* or *Qtiplot* project upon reasonable request from the authors. All computed structures are deposited on the ioCHEM-BD online repository and can be accessed freely.

Supporting Information

Investigating Halogen-Bond-Mediated Through-Space Activation of CO_2 for Electrocatalytic Reduction by Iron Porphyrins

Cecilia Albanese,[a,d] Sihem Groni,[b,d] Lauriane Chevalier,[d] Gabriele Di Carlo,[a] Francesca Tessore,*[a] Marc Robert,[b,d,e] Bernd Schöllhorn,[c] Niklas von Wolff,*[b] and Claire Fave*[b,d]

[a.] *Department of Chemistry, University of Milano, INSTM RU, via Golgi 19, 20133 Milano, Italy.*
[b.] *Sorbonne Université, CNRS, Institut Parisien de Chimie Moléculaire, IPCM, Paris F-75005, France.*
[c.] *Université Paris Cité, ITODYS, F-75013 Paris, France*
[d.] *Université Paris Cité, F-75013 Paris, France*
[e.] *Institut Universitaire de France (IUF), F-75005, Paris, France.*

Table of Contents

1 General Remarks

1.1 Chemicals

All reactions were performed under exclusion of air and water using oven dried flasks, dry solvents, and argon gas, unless otherwise noted. Small volumes for reactions were transferred. Thin layer chromatography (TLC) was performed on Merck TLC aluminium sheets (silica gel 60, F254) and column chromatography with silica gel.

Chemicals were bought from TCI, Alfa Aesar, Merck and Sigma Aldrich and used without further purification unless stated otherwise: 1H-Pyrrole Azole Divinylenimine Imidole (Sigma Aldrich) was distilled under reduced pressure and used immediately, 2-Bromobenzaldehyde (TCI), 2-Bromo-4-fluorobenzaldehyde (TCI), 2-Bromo-6-fluorobenzaldehyde (Sigma Aldrich), 2,3-Dichloro-5,6-dicyano-1,4-benzoquinone (ALFA AESAR), Boron trifluoride diethyl etherate $BF_3(OEt)_2$ (Sigma Aldrich), Triethylamine (Sigma Aldrich), Indium(III) trifluoromethanesulfonate (Merck), $TBAPF_6$ (Sigma Aldrich). Dimethyl formamide (DMF) was bought in peptide grade quality. Dichloromethane was distilled over CaH_2 under Argon. The porphyrins **FeTPP**, **FeF20TPP** (Sigma Aldrich) and **FeTolylTPP** (Por-Lab GMBH).

1.2 Apparatus

NMR spectra were recorded on the following Brucker devices: DRX-400 (400 MHz). Shifts are given in parts per million (ppm). The generated data was analyzed with TopSpin, MestReNova 6 and Bindfit.

Cyclic voltammetry experiments were performed using an Metrohm Autolab potentiostat. For CVs, a conventional one-compartment three-electrode electrochemical cell was used. GC disk (1 mm diameter) electrode was used as working electrode (WE), platinum wire was employed as counter (CE) electrode and a salt bridge containing the electrolyte was used to connect the electrochemical cell with saturated calomel (SCE) reference electrode (RE). The electrolyte solution was purged with argon flow for few minutes prior to any electrochemical measurement. The absence of oxygen traces was confirmed by a background cyclic voltammetry measurement. Unless otherwise stated, all measurements were performed at room temperature (20 °C).

2 Synthesis and Characterisations

2.1 Synthesis of free-base porphyrins

2.1.1 Synthesis of **1**

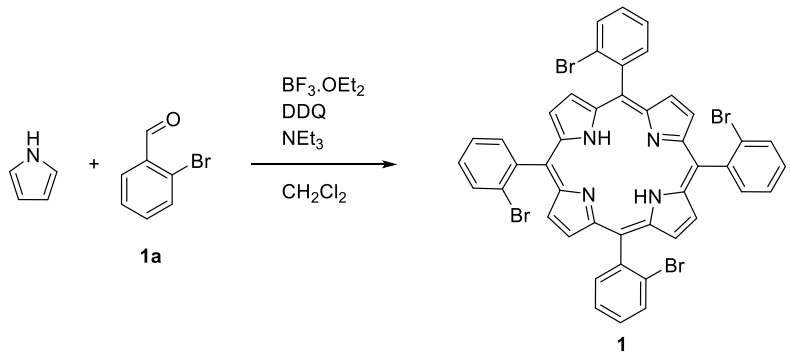

In a dry two neck round-bottom flask, 150 µL of **1a** (1.29 mmol, 1 equivalent) were dissolved, under Ar flow, in 150 mL of dry CH_2Cl_2. 89.5 µL of freshly distilled pyrrole (1.29 mmol, 1 equivalent) were added to the solution. The round bottomed flask was then covered with aluminium foil to protect the reaction from ambient light, and 48 µL of $BF_3(OEt)_2$ (0.39 mmol, 0.3 equivalents) were added to the solution. The reaction was allowed to stir in dark, under argon atmosphere, at RT for 16 hours. After that time the aluminium foil and the argon flow were removed, 220 mg of DDQ (0.97 mmol, 0.75 equivalents) were added and the reaction was stirred 4 hours at RT exposed to air and ambient light. Finally, 180 µL of triethylamine (1.29 mmol, 1 equivalent) were added to the solution and let stir for 1 hour. The crude was retrieved evaporating the solvent *in vacuo*, and the solid obtained was purified by gravimetric chromatography (eluent from CH_2Cl_2/n-hexane = 1/1 to CH_2Cl_2/n-hexane = 3/1) affording compound **1** as a purple powder (34 mg, 12% yield). ^{1}H NMR (400 MHz, $CDCl_3$) δ: 8.60 (s, 8H, H_β pyrrolic), 8.14-7.91 (m, 8H, Ar-H), 7.67-7.51 (m, 8H, Ar-H), -2.70 (s, 2H, NH).

2.1.2 Synthesis of **2**

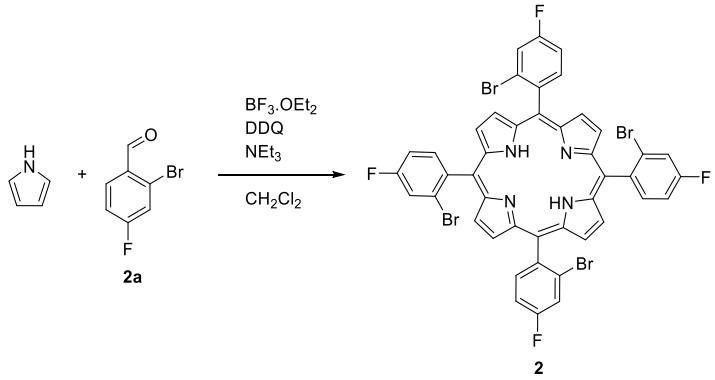

In a dry two neck round-bottom flask, 200 mg of **2a** (0.98 mmol, 1 equivalent) were dissolved, under Ar flow, in 125 mL of dry CH_2Cl_2. 68.0 µL of freshly distilled pyrrole (0.98 mmol, 1 equivalent) were added to the solution. The round bottomed flask was then covered with aluminium foil to protect the reaction from ambient light, and 36 µL of $BF_3(OEt)_2$ (0.29 mmol, 0.3 equivalents) were added to the solution. The reaction was allowed to stir in dark, under argon atmosphere, at RT for 16 hours. After that time the aluminium foil and the argon flow were removed, 167 mg of DDQ (0.74 mmol, 0.75 equivalents) were added and the reaction was stirred 4 hours at RT exposed to air and ambient light. Finally, 137 µL of triethylamine (0.98 mmol, 1 equivalent) were added to the solution and let stir for

1 hour. The crude was retrieved evaporating the solvent in vacuo, and the solid obtained was purified by gravimetric chromatography (eluent CH_2Cl_2/n-hexane = 1/1) affording compound **2** as a purple powder (104 mg, 40% yield). ^{1}H NMR (400 MHz, $CDCl_3$) δ: 8.60 (s, 8H, H_β pyrrolic), 8.18-7.93 (m, 4H, Ar-H), 7.70 (m, 4H, Ar-H), 7.38-7.28 (m, 4H, Ar-H), -2.77 (s, 2H, NH).^{19}F NMR (376 MHz, $CDCl_3$) δ: -111.29 (s, 4F).

2.1.3 Synthesis of **3**

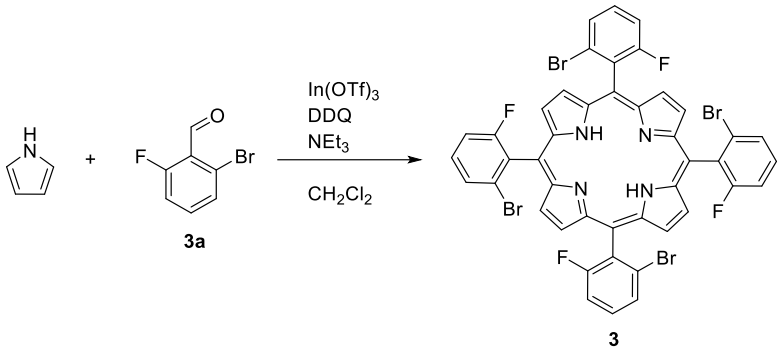

In a dry two neck round-bottom flask, 250 mg of **3a** (1.23 mmol, 1 equivalent) were dissolved, under argon flow, in 125 mL of dry CH_2Cl_2. 85.0 µL of freshly distilled pyrrole (1.23 mmol, 1 equivalent) were added to the solution. The round bottomed flask was then covered with aluminium foil to protect the reaction from ambient light, and 41.5 mg of $In(OTf)_3$ (0.07 mmol, 0.06 equivalents) were added to the solution. The reaction was allowed to stir in dark, under argon atmosphere, at RT for 24 hours. After that time the aluminium foil and the argon flow were removed, 167 mg of DDQ (0.74 mmol, 1.5 equivalents) were added and the reaction was stirred 4 hours at RT exposed to air and ambient light. Finally, 342 µL of triethylamine (2.46 mmol, 2 equivalent) were added to the solution and let stir for overnight. The crude was retrieved evaporating the solvent in vacuo, and the solid obtained was purified by gravimetric chromatography (eluent CH_2Cl_2/n-hexane = 3/1) affording compound **3** as a purple powder (12.5 mg, 4% yield). ^{1}H NMR (400 MHz, $CDCl_3$) δ: 8.66 (s, 8H, H_β pyrrolic), 7.80 (m, 4H, Ar-H), 7.61 (m, 4H, Ar-H), 7.46-7.40 (m, 4H, Ar-H), -2.70 (s, 2H, NH). ^{19}F NMR (376 MHz, $CDCl_3$) δ: -103.44 (m, 4F).

2.1.4 Synthesis of **4**

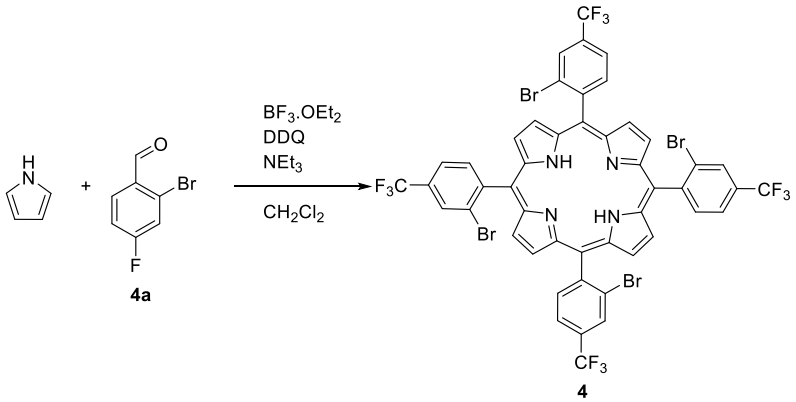

In a dry two neck round-bottom flask, 119 *µL* of **4a** (0.79 mmol, 1 equivalent) were dissolved, under argon flow, in 125 mL of dry CH_2Cl_2. 55.0 µL of freshly distilled pyrrole (0.79 mmol, 1 equivalent) were added to the solution. The round bottomed flask was then covered with aluminium foil to protect the reaction from ambient light, and 36 µL of $BF_3(OEt)_2$ (0.29 mmol, 0.3 equivalents) were added to the solution. The reaction was allowed to stir in dark, under argon atmosphere, at RT for 16 hours. After that time the aluminium foil and the argon flow were removed, 167 mg of DDQ (0.74 mmol, 0.75 equivalents) were added and the reaction was stirred 4 hours at RT exposed to air and

ambient light. Finally, 137 µL of triethylamine (0.98 mmol, 1 equivalent) were added to the solution and let stir for 1 hour. The crude was retrieved evaporating the solvent in vacuo, and the solid obtained was purified by gravimetric chromatography (eluent CH_2Cl_2/n-hexane = 1/1) affording compound **4** as a purple powder (45 mg, 19% yield). ^{1}H NMR (400 MHz, $CDCl_3$) δ: 8.57 (s, 8H, H_β pyrrolic), 8.30-8.10 (m, 8H, Ar-H), 7.88 (m, 4H, Ar-H), -2.74 (s, 2H, NH). ^{19}F NMR (376 MHz, $CDCl_3$) δ: -62.27 (m, 12F).

2.2 Synthesis of iron porphyrins

2.2.1 General procedure for the synthesis of iron complexes **1-Fe** to **5-Fe**

In a microwave vessel equipped with a stirring bar, the appropriate free-base porphyrin (1 mmol) was dissolved in dry DMF (5 mL) and Ar was bubbled into the solution. After 5 minutes bubbling, $FeBr_2$ (5 mmol) was added to the solution. The vessel was then sealed and heated under microwave irradiation (150 °C) for 15 min. After cooling down at room temperature the DMF solution was added dropwise to 15 mL of a 6M HCl_{aq}, causing the precipitation of the iron chloride porphyrin, which was collected by filtration. The solid was washed first with HCl_{aq} 3M and then several time with water. After carefully drying under vacuum, porphyrin **1-Fe** to **5-Fe** were collected in almost quantitatively yield as dark brownish solids.

2.2.2 Synthesis of **1Fe**

Yield: 98%

^{1}H NMR (400 MHz, $CDCl_3$) δ: 79.37 (s, 8H, H_β pyrrolic), 13.05 (s, 8H, Ar-H), 12.46-11.56 (m, 8H, Ar-H)

Mass-ESI+: m/z = 983.80051 $[M\text{-}Cl]^+$

2.2.3 Synthesis of **2Fe**

Yield: 87%

^{1}H NMR (400 MHz, $CDCl_3$) δ: 80.74 (s, 8H, H_β pyrrolic), 16.34-6.09 (m, 12H, Ar-H)

^{19}F NMR (376 MHz, $CDCl_3$) δ: -106.66 (s, 4F)

Mass-ESI+: m/z = 1087.78662 $[M+H]^+$

2.2.4 Synthesis of **3Fe**

Yield: 95%

^{1}H NMR (400 MHz, $CDCl_3$) δ: 81.44 (s, 8H, H_β pyrrolic), 12.80-10.15 (m, 12H)

^{19}F NMR (376 MHz, $CDCl_3$) δ: -99.67 (m, 4F)

2.2.5 Synthesis of **4Fe**

Yield: 94%

^{1}H NMR (400 MHz, $CDCl_3$) δ: 80.15 (s, 8H, $_\beta$ pyrrolic), 13.63-12.81 (m, 4H, Ar-H), 12.49-11.75 (m, 4H, Ar-H), 11.05 (s, 4H, Ar-H)

^{19}F NMR (376 MHz, $CDCl_3$) δ: -59.92 (m, 12F)

Mass-ESI+: *m/z* = 1256.20 $[M\text{-}Cl]^+$

2.2.6 Synthesis of **5Fe**

Yield: 98%

^{1}H NMR (400 MHz, $CDCl_3$) δ: 80.41 (s, 8H), 13.32 (s, 7H), 12.22 (s, 7H)

Mass-ESI+: *m/z* = 940.30 $[M\text{-}Cl]^+$

3 Electrochemical Characterization of the iron porphyrin by CV

3.1 CVs of iodinated compounds:

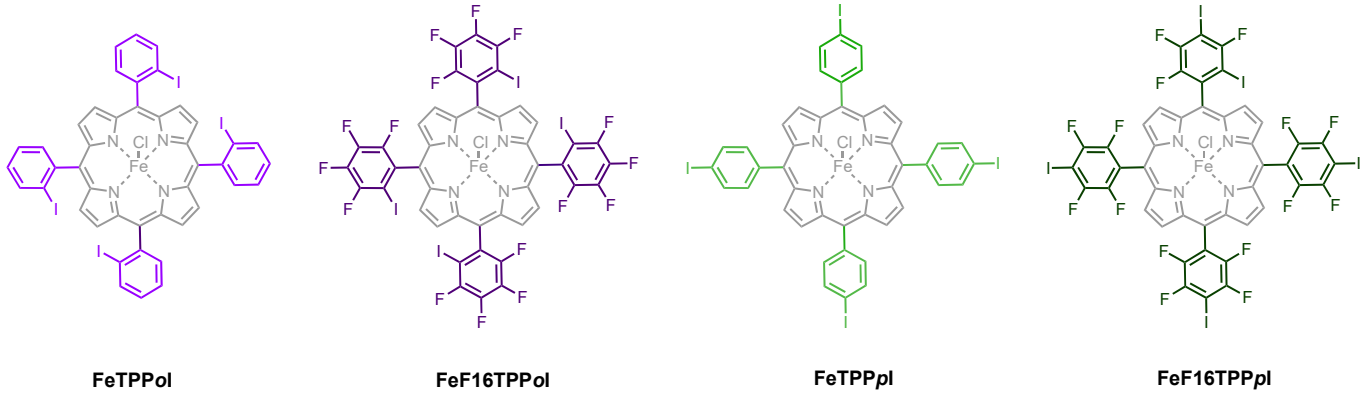

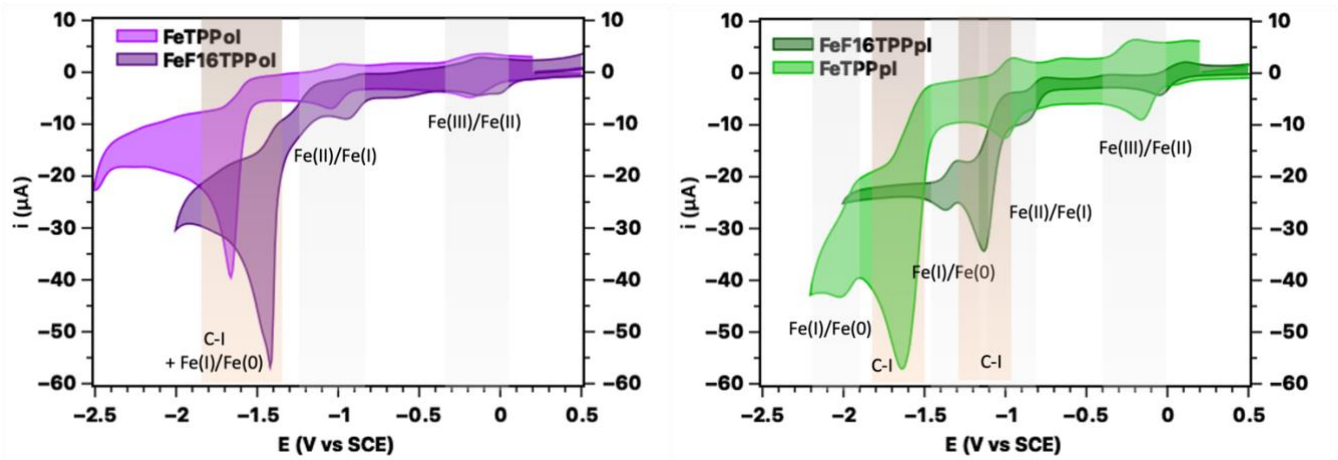

Figure S1: CVs under Ar of *ortho*-iodinated iron porphyrins **FeTPP*o*I** and **FeF16TPP*o*I** (left) and of *para*-iodinated porphyrins **FeTPP*p*I** and **FeF16TPP*p*I** (right) in 0.1 M $TBAPF_6$/DMF, ν = 100 $mV.s^{-1}$, c = 0.5 mM.

3.2 CVs of compounds 3Fe

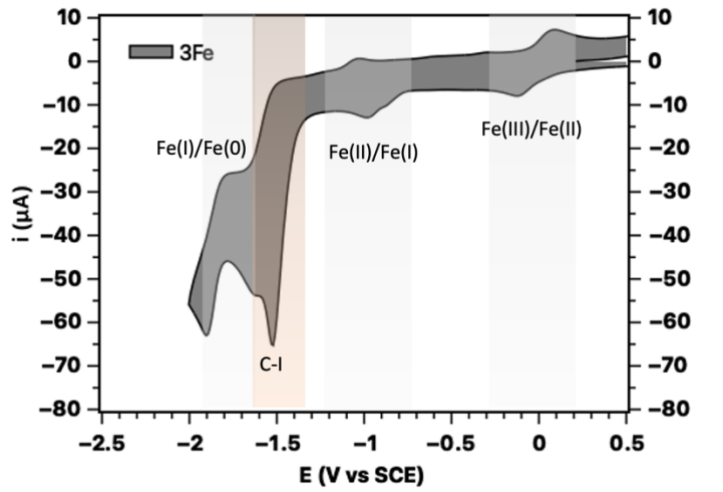

Figure S2: CVs of **3Fe** under Ar in 0.1 M $TBAPF_6$/DMF, ν = 100 $mV.s^{-1}$, c = 0.5 mM.

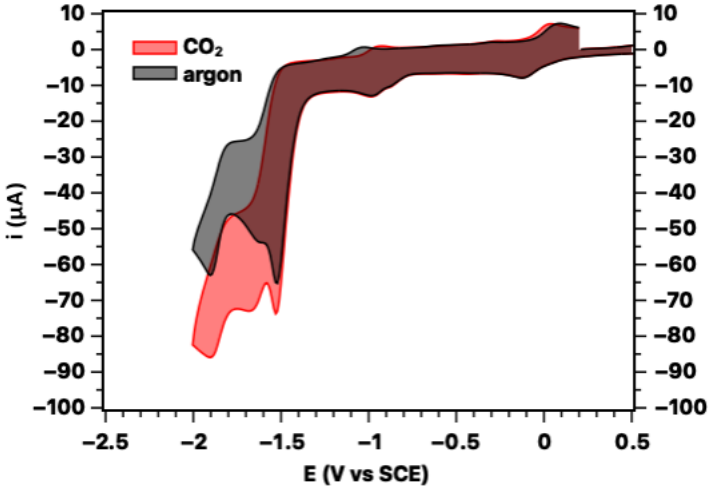

Figure S3: CVs of **3Fe** in 0.1 M $TBAPF_6$/DMF, ν = 100 $mV.s^{-1}$, c = 0.5 mM. Black line: under Ar; red line: under CO_2.

3.3 CV of compound 5Fe:

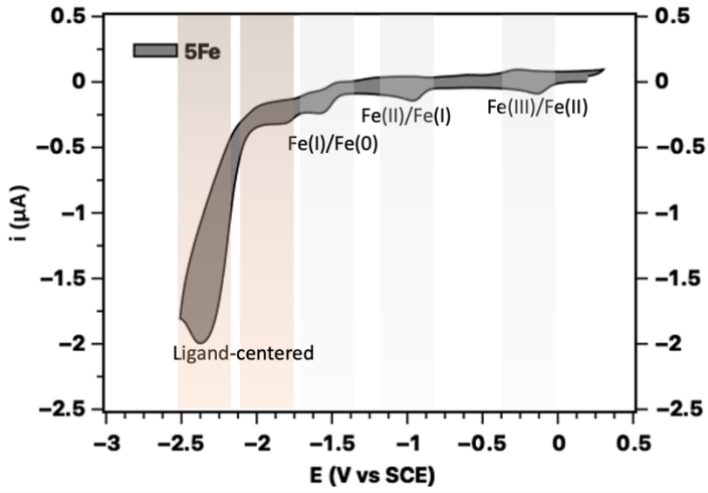

Figure S4: CVs of **5Fe** under Ar in 0.1 M $TBAPF_6$/DMF, ν = 100 $mV.s^{-1}$, c = 0.5 mM

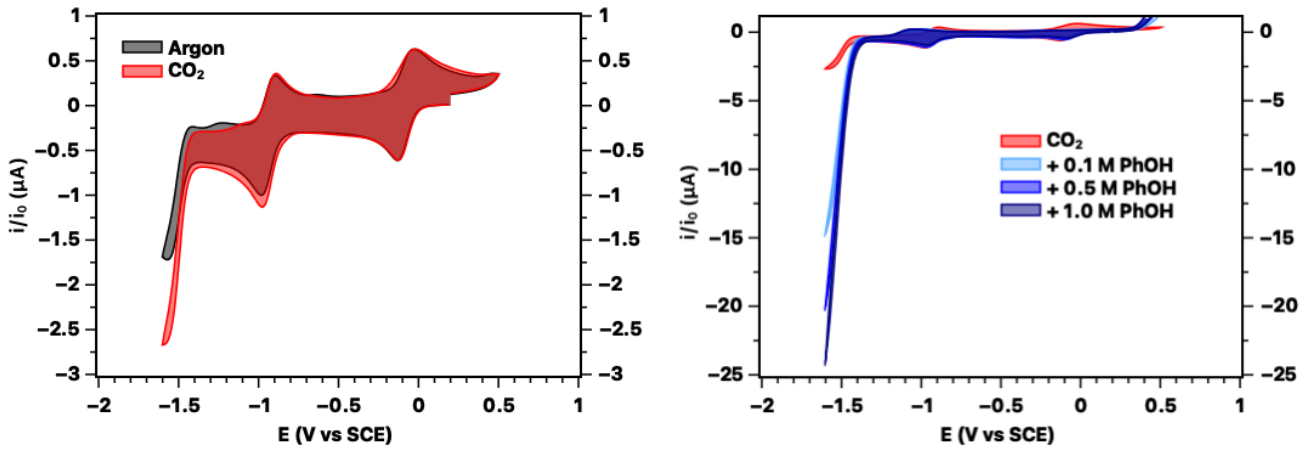

Figure S5: CVs of **5Fe** under CO_2 in 0.1 M $TBAPF_6$/DMF, ν = 100 mV.s^{-1}, c = 0.5 mM (left) and under CO_2 (right) in the presence of varying concentrations of PhOH (0.1, 0.5 and 1 M PhOH).

3.4 CVs under Argon

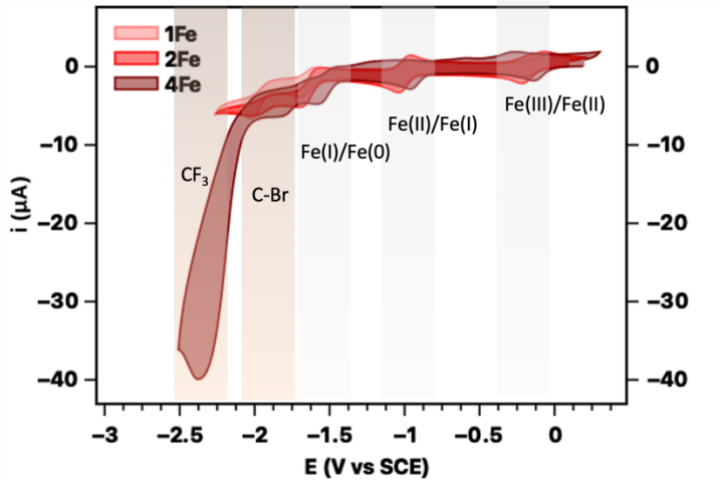

Figure S6: CVs of **1Fe, 2Fe** and **4Fe** under argon in 0.1 M $TBAPF_6$/DMF, ν = 100 mV.s^{-1}, c = 0.5 mM, showing C-Br and CF_3 (**4Fe**) cleavage after the Fe(I)/Fe(0) wave.

3.5 CVs under CO_2

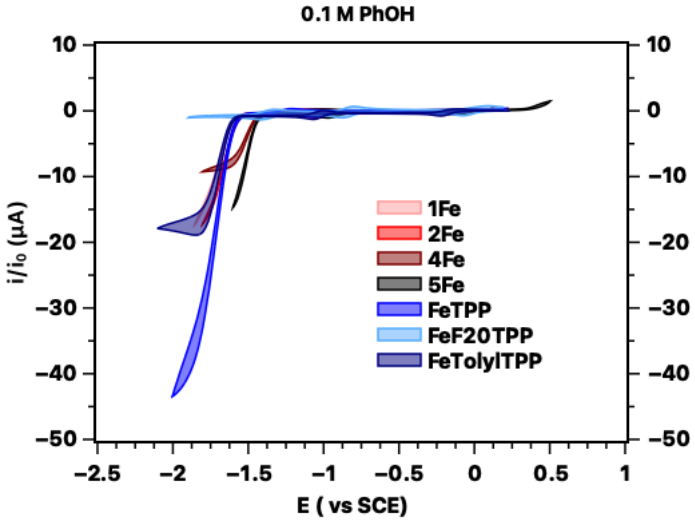

Figure S7: CVs under CO_2 in 0.1 M $TBAPF_6$/DMF ν = 100 mV. s^{-1}, c= 0.5 mM in presence of 0.1M of PhOH.

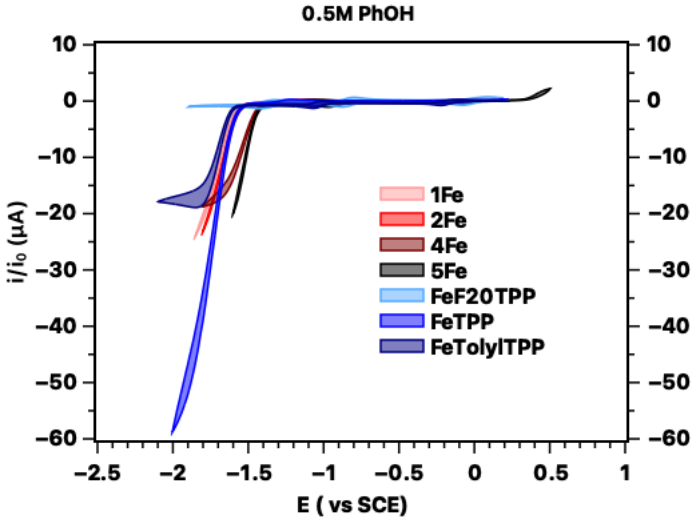

Figure S8: CVs under CO_2 in 0.1 M $TBAPF_6$/DMF ν = 100 mV. s^{-1}, c= 0.5 mM in presence of 0.5 M of PhOH.

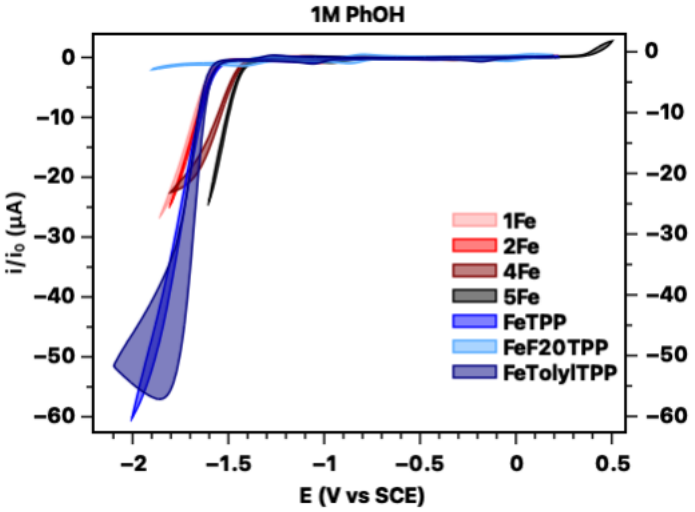

Figure S9: CVs under CO_2 in 0.1 M $TBAPF_6$/DMF ν = 100 mV.s^{-1}, c= 0.5 mM in presence of 1.0 M of PhOH.

4 Electrochemical CO_2-to-CO conversion

4.1 Controlled potential electrolysis (CPE) procedure

The electrolysis experiments were conducted in 0.1 M TBAPF6/DMF, at a concentration of 0.5 mM of porphyrin, adding 500 equivalents of phenol (total volume of the solution 3 mL) in a three-electrode set-up. A glassy carbon plate (surface = 2.4 cm^2) was used as working electrode, a Pt-grid as counter electrode and a Saturated Calomel Electrode (SCE) as reference. The stability of the porphyrins during the experiment were evaluated by recording a CV before and after the one-hour electrolysis. No major changes in the CV signals were observed. A slight decrease of the Faradic Efficiency of 1 to 17 % can be attributed to minor degradation of the catalysts. The experiments confirmed that all four porphyrins are selectively active for the catalytic reduction of CO_2 to CO at potentials corresponding to the Fe(I)/Fe(0) redox couple without forming H_2.

4.2 CPEs at -1.7 V *vs* SCE

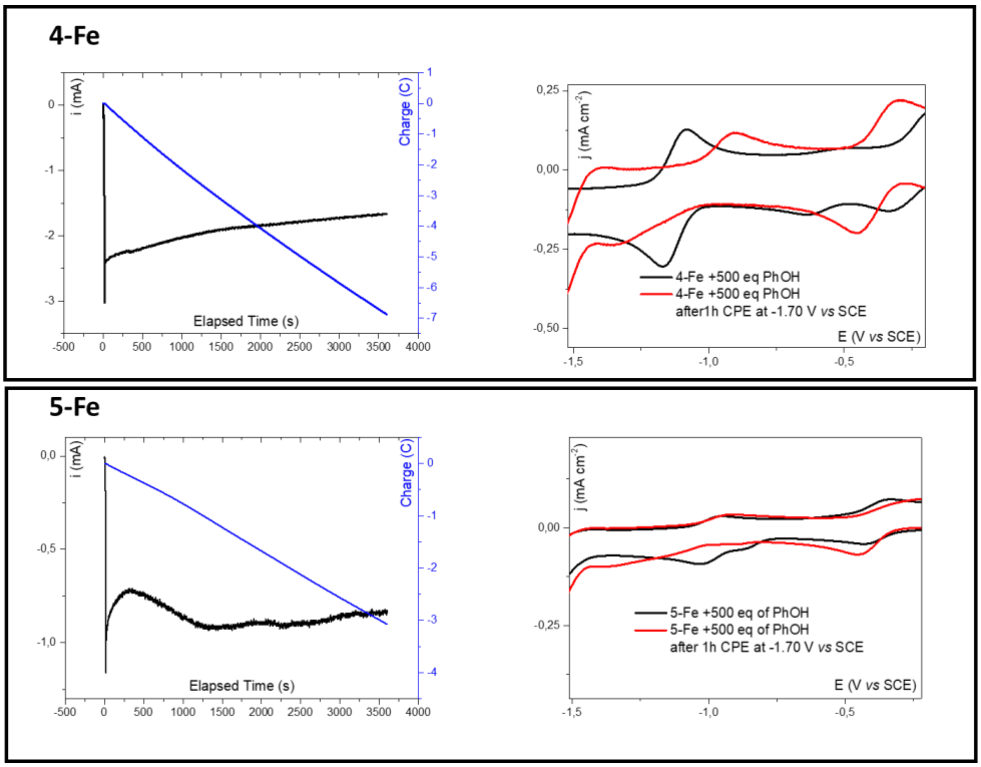

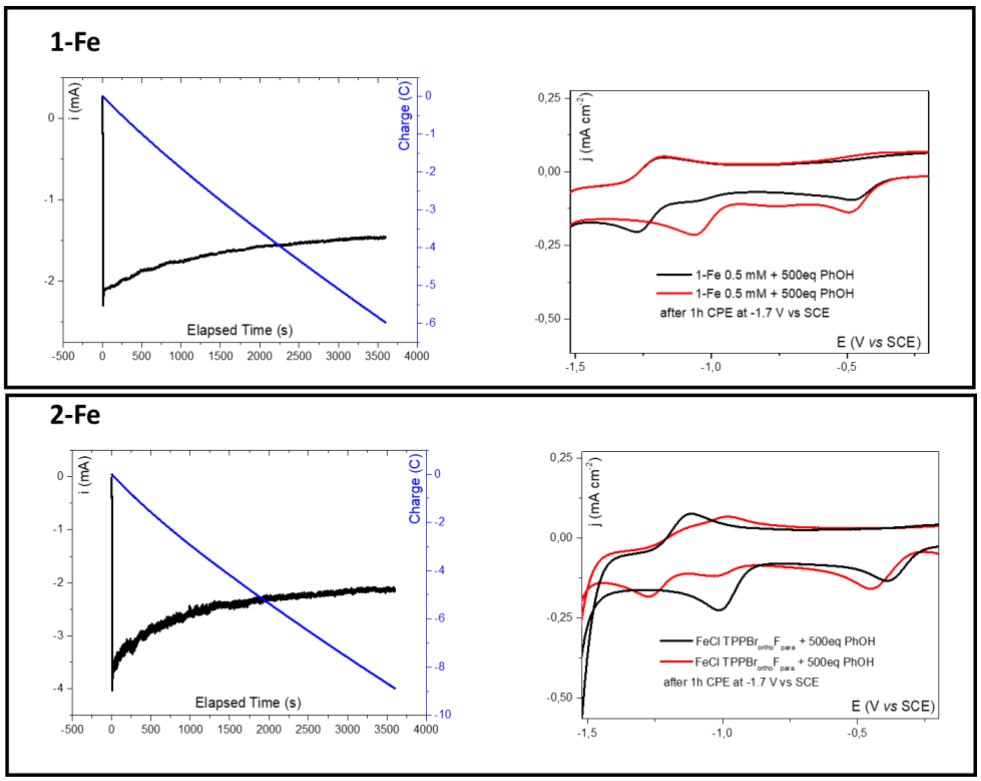

Figure S10: Current (black) and charge (blue) traces (left), as well as CVs before (black) and after (red) 1 h electrolysis at -1.7 V vs SCE (right) of the different iron porphyrins.

Table S1: Calculated faradaic efficiencies (FE) for H_2 and CO after 1h electrolysis at – 1.70 V vs SCE. No other liquid products have been observed.

Catalyst	FE H_2	FE CO
1Fe	0 %	92 %
2Fe	0 %	87 %
4Fe	0 %	83 %
5Fe	0%	99 %

5 FOTWA-Analysis

5.1 Kinetic analysis

The kinetic constants were obtained by applying the FOTWA formalisms that links normalized currents to the rate constant according to[1]:

$$\frac{i}{i_0} = \frac{2.24\sqrt{\frac{k_{cat}}{fv}C_A^0}}{1 + exp[f(E - E_{cat}^0)]}$$

The rate constants can then be obtained by fitting the linear part of catalytic CVs (at $|E| \ll |E_{cat}^0|$) to a plot of i/i_0 *vs* $\frac{1}{1+exp[f(E-E_{cat}^0)]}$. The slope of the FOTWA analysis then links to the rate constant according to[1]:

$$slope = 2.24\sqrt{\frac{k_{cat}}{fv}C_A^0}$$

and thus:

$$k_{cat}\ [s^{-1}M^{-1}] = \left(\frac{slope}{2.24}\right)^2 \frac{fv}{C_A^0}$$

with $C_A^0 = 0.23\ M$,[2] the concentration of CO_2 in DMF, $f = \frac{F}{RT}$ and $v = 0.1\ V/s$, the scan rate of the experiments. F, R and T are the Faraday constant, Gas constant and temperature. As not all values of i_0 were obtainable (quasi-reversible Fe(I)/Fe(0) transitions), we normalized all CVs throughout with i_0', the current of the Fe(II)/Fe(I) transition, that was reversible in all cases. This approximation is reasonable as the diffusion coefficients at the Fe(I) and Fe(I) level, and hence currents, are almost identical. For example, for **FeTPP**, the diffusion coefficients at the Fe(II)/(I) wave and the Fe(I)/(0) wave are 2.7 x 10^{-6} and 3.2 x 10^{-6} cm^2s^{-1} respectively.[3]

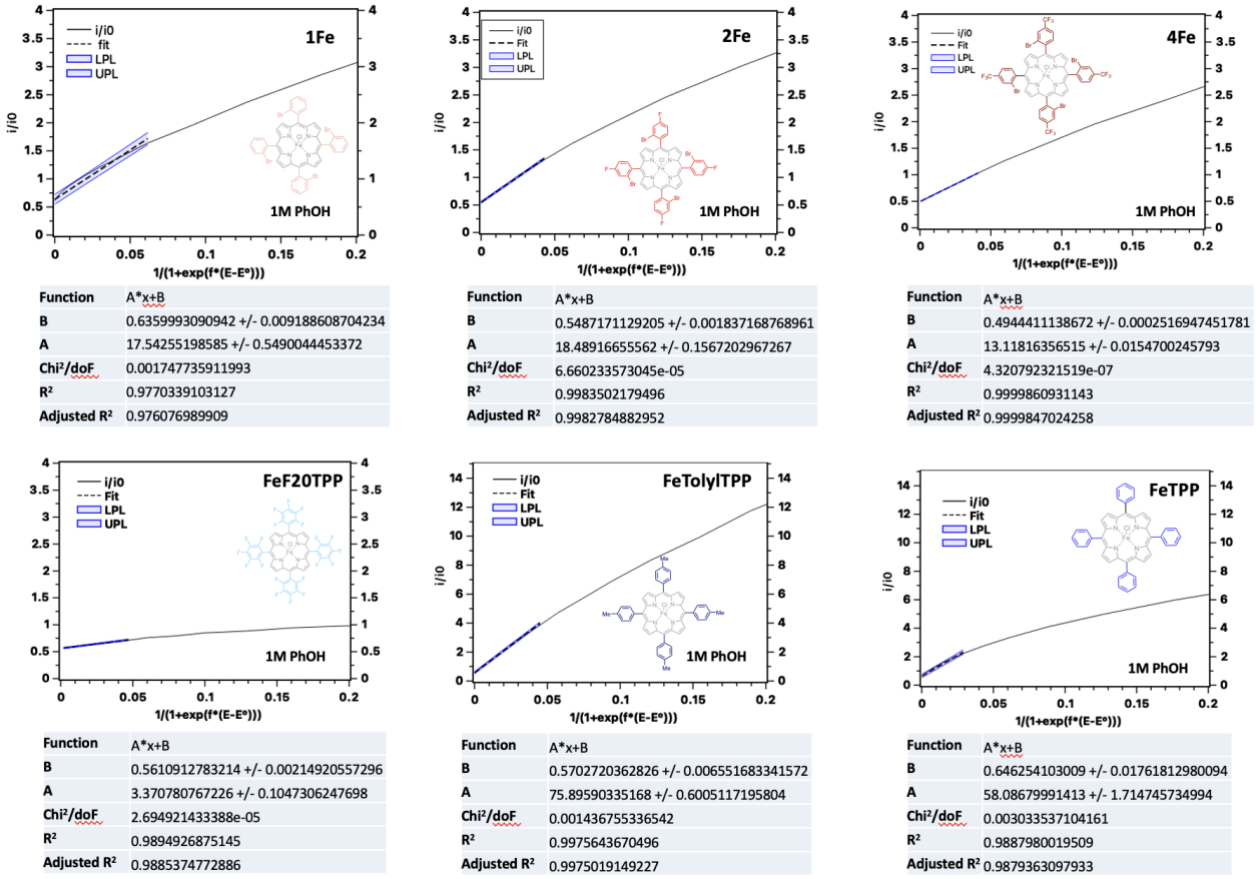

Figure S11: FOTWA plots of the different compounds investigated. Linear fits were performed for values of $\frac{1}{1+exp[f(E-E^0_{cat})]}$ below 0.05, in the initial linear region of the plots.

5.2 Error-propagation

In order to clearly asses if the different compounds follow the linear trend of E^0_{cat} *vs* $\log(k_{cat})$ or if on the other hand, they lay outside this range, it is necessary to get an idea of the standard deviation on both k_{cat} and $\log(k_{cat})$. The error on k_{cat} was estimated as:

$$\sigma_k = 2k_{cat} \cdot \frac{\sigma_m}{m}$$

with σ_m the standard error of the slope m of the FOTWA plot. The error for the E^0_{cat} *vs* $\log(k_{cat})$ plot then is obtained according to:

$$\sigma_{log} = \frac{1/f}{k_{cat}}\sigma_k$$

with f and σ_k defined as above.

5.3 Catalytic Tafel plots

Catalytic Tafel plots were constructed using the k_{cat} values from the FOTWA analysis. The TOF values were obtained according to:[1,2]

$$TOF = \frac{TOF_{max}}{1 + exp[f(E^0_{tr} - E^0_{cat})] \times exp[-f\eta]}$$

With f as defined above and with η defined as:

$$\eta = \pm(E_{tr}^{0} - E) \qquad (+ \text{ for reductions}, - \text{ for oxidations})$$

With TOF_{max} defined as:

$$TOF_{max}\,[s^{-1}] = k_{cat} \times C_{CO_2}^{0}$$

Where $C_{CO_2}^{0}$ is the concentration of CO_2 in DMF, which is taken as 0.23 M.[2]

With E_{tr}^{0} being the standard potential of the target reaction. We assumed here:

$$E_{tr}^{0} = E_{CO_2/CO,DMF}^{0} = -0.74\ V\ vs\ SHE$$

This value is strictly speaking only valid in the presence of water (as strongest proton donor), but was adapted for ease of calculation. The value for E_{tr}^{0} was taken as:

$$E_{tr}^{0} = E_{CO_2/CO,DMF}^{0} = -0.981\ V\ vs\ SCE$$

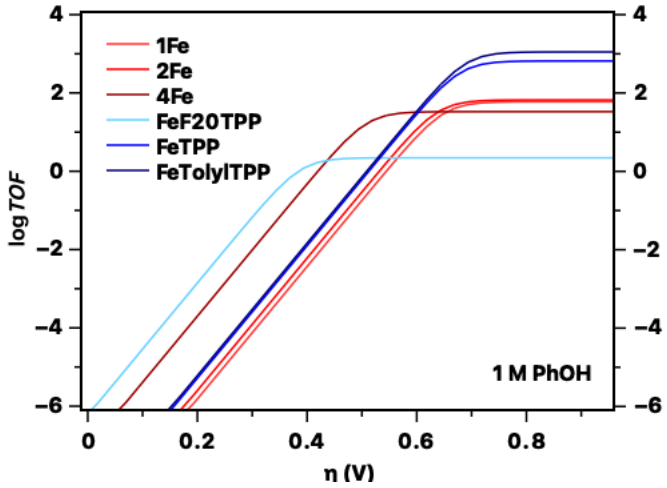

Figure S12: Catalytic Tafel plots of the Fe-porphyrins in the presence of 1M of PhOH.

6 DFT Calculations

6.1 General

Optimizations and frequency calculations were done using the Gaussian 16 software suite in the B.01 revision (Gaussian 16, Revision B.01, M. J. Frisch, G. W. Trucks, H. B. Schlegel, G. E. Scuseria, M. A. Robb, J. R. Cheeseman, G. Scalmani, V. Barone, G. A. Petersson, H. Nakatsuji, X. Li, M. Caricato, A. V. Marenich, J. Bloino, B. G. Janesko, R. Gomperts, B. Mennucci, H. P. Hratchian, J. V. Ortiz, A. F. Izmaylov, J. L. Sonnenberg, D. Williams-Young, F. Ding, F. Lipparini, F. Egidi, J. Goings, B. Peng, A. Petrone, T. Henderson, D. Ranasinghe, V. G. Zakrzewski, J. Gao, N. Rega, G. Zheng, W. Liang, M. Hada, M. Ehara, K. Toyota, R. Fukuda, J. Hasegawa, M. Ishida, T. Nakajima, Y. Honda, O. Kitao, H. Nakai, T. Vreven, K. Throssell, J. A. Montgomery, Jr., J. E. Peralta, F. Ogliaro, M. J. Bearpark, J. J. Heyd, E. N. Brothers, K. N. Kudin, V. N. Staroverov, T. A. Keith, R. Kobayashi, J. Normand, K. Raghavachari, A. P. Rendell, J. C. Burant, S. S. Iyengar, J. Tomasi, M. Cossi, J. M. Millam, M. Klene, C. Adamo, R. Cammi, J. W. Ochterski, R. L. Martin, K. Morokuma, O. Farkas, J. B. Foresman, and D. J. Fox, Gaussian, Inc., Wallingford CT, 2016). Single point energy

calculations were performed using the ORCA Software (6.1.1).[4] Molecular visualization was carried out using Chemcraft (https://www.chemcraftprog.com).

All geometries were optimized using the M06-L functional,[5] the def2-SVP basis set[6] and W06 density fitting to increase computational efficiency,[7] as well as Grimme's empirical GD3 dispersion correction.[8] All structures were optimized in solution (DMF) using the integral equation formalism variant (IEFPCM) of the PCM model in the SMD variation of Truhlar and co-workers.[9] Frequency calculations at this level of theory confirmed stationary points and transition states and were used to compute thermodynamic properties at 298.15K, if not stated otherwise. Single point energies of the optimized structures were computed (with solvation SMD=DMF)[9] using the range-separated hybrid meta-GGA exchange-correlation functional ωB97M-V[10] including non-local correlation (VV10),[11,12] together with the triple-ζ def2-TZVPP basis set[6] and density fitting with the RIJCOSX formalism using the auxiliary basis sets def2/J[7] and def2-TZVPP/C[13] to speed up computational time. The choice of the ωB97M-V functional was rationalized given its excellent results in a recent benchmark study on transition metal reactions.[14]

6.2 ESP mapping

The electrostatic potential maps were constructed from the electron-density obtained from the single point ORCA jobs. The ORCA standalone orca_plot utility was used to generate then the corresponding electrostatic potential surface as a 3D Gaussian cube file with 200 grid intervals. A home-made script was then used to compute the ESP values at a specific iso-value of the energy density (in general 0.001).[15] The parameters used in the script to obtain the sigma-hole values and ESP surfaces (as pqr files) are the following:

$$isosurface\ value = 0.001$$

$$Radius\ for\ local\ extrama\ detection = 0.1\ \text{Å}$$

$$Maximal\ distance\ from\ halogen\ atom\ for\ extrema\ detection = 0.2\ \text{Å}$$

$$Maximal\ angle\ of\ the\ cone\ along\ the\ C-X\ axis\ for\ extrema\ detection = 40°$$

The ESP surfaces (from the pqr-files) were then visualized with VMD[16] 1.9.4a57 (https://www.ks.uiuc.edu/Research/vmd/).

6.3 Structures

All computed structures are deposited on the ioCHEM-BD online repository and can be accessed freely.

7 References

1 C. Costentin, S. Drouet, M. Robert and J.-M. Savéant, *J. Am. Chem. Soc.*, 2012, **134**, 11235–11242.

2 I. Azcarate, C. Costentin, M. Robert and J.-M. Savéant, *J. Phys. Chem. C*, 2016, **120**, 28951–28960.

3 N. H. Mitchell and N. Elgrishi, *J. Phys. Chem. C*, 2023, **127**, 10938–10946.

4 F. Neese, *WIREs Comput. Mol. Sci.*, 2025, **15**, e70019.

5 Y. Zhao and D. G. Truhlar, *J. Chem. Phys.*, 2006, **125**, 194101.

6 F. Weigend and R. Ahlrichs, *Phys. Chem. Chem. Phys.*, 2005, **7**, 3297–3305.

7 F. Weigend, *Phys. Chem. Chem. Phys.*, 2006, **8**, 1057–1065.

8 S. Grimme, J. Antony, S. Ehrlich and H. Krieg, *J. Chem. Phys.*, 2010, **132**, 154104.

9 A. V. Marenich, C. J. Cramer and D. G. Truhlar, *J. Phys. Chem. B*, 2009, **113**, 6378–6396.

10 N. Mardirossian and M. Head-Gordon, *J. Chem. Phys.*, 2016, **144**, 214110.

11 O. A. Vydrov and T. Van Voorhis, *J. Chem. Phys.*, 2010, **133**, 244103.

12 W. Hujo and S. Grimme, *J. Chem. Theory Comput.*, 2011, **7**, 3866–3871.

13 A. Hellweg, C. Hättig, S. Höfener and W. Klopper, *Theor. Chem. Acc.*, 2007, **117**, 587–597.

14 M. A. Iron and T. Janes, *J. Phys. Chem. A*, 2019, **123**, 3761–3781.

15 N. von Wolff, nvonwolff/Sigma-Hole-Analysis Zenodo 2026.

16 W. Humphrey, A. Dalke and K. Schulten, *J. Mol. Graph.*, 1996, **14**, 33–38.

8 Spectra of compounds

8.1 Free-base porphyrins

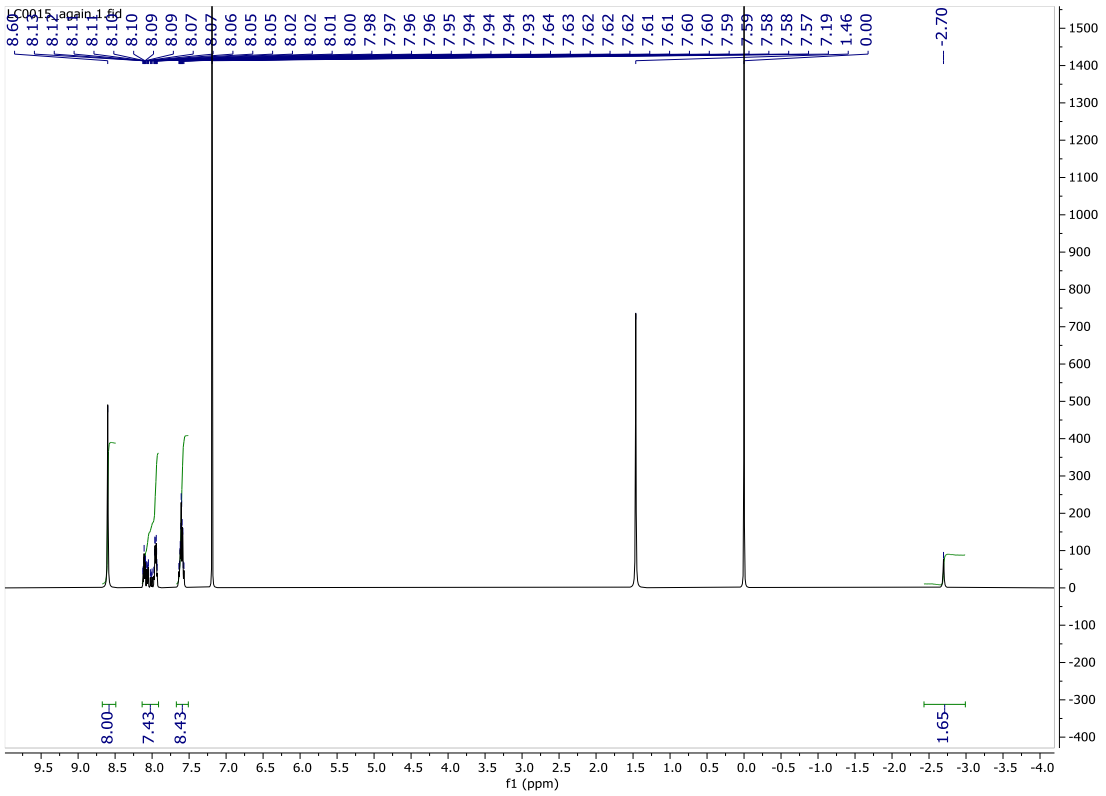

Figure S13: ^{1}H NMR in $CDCl_3$ of **1**

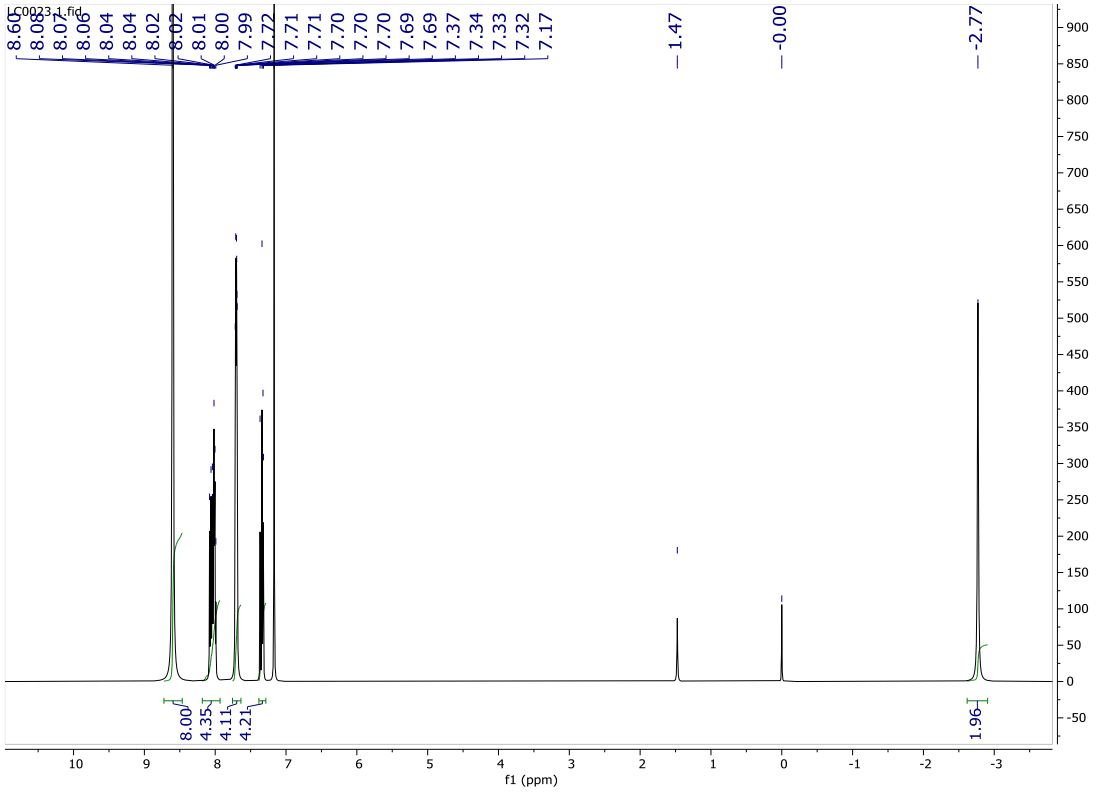

Figure S14: ^{1}H NMR in $CDCl_3$ of **2**

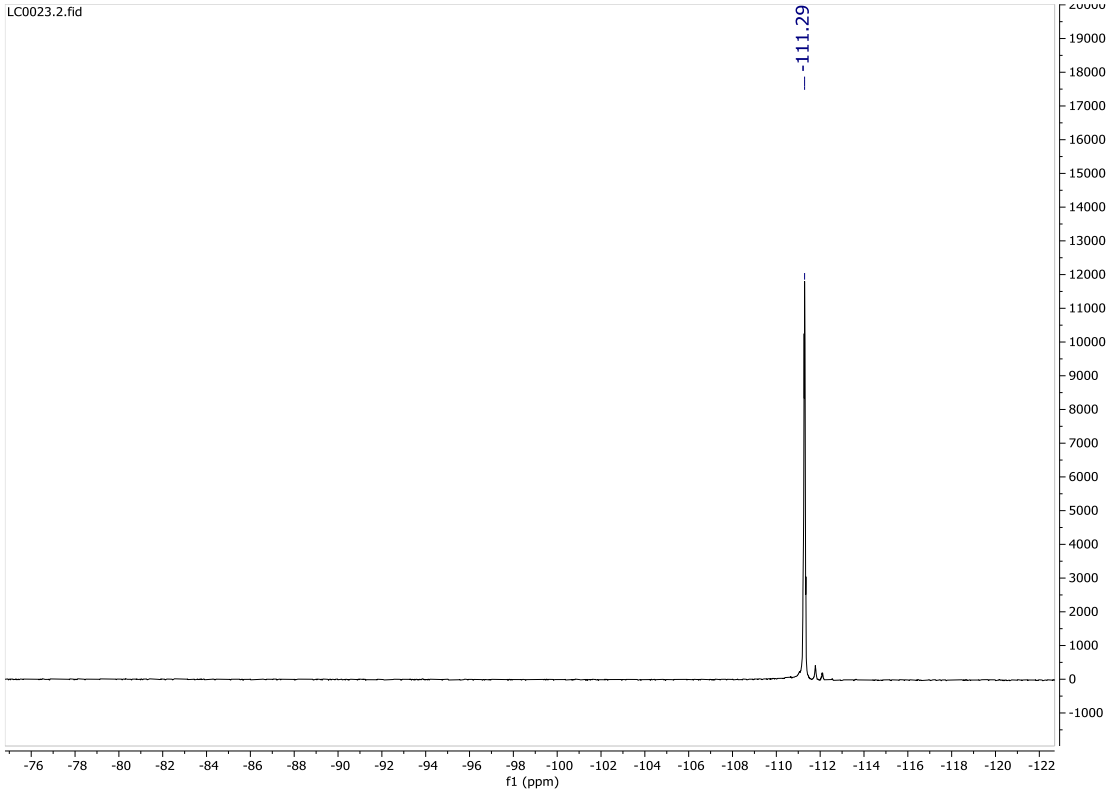

Figure S15: ^{19}F NMR in $CDCl_3$ of **2**

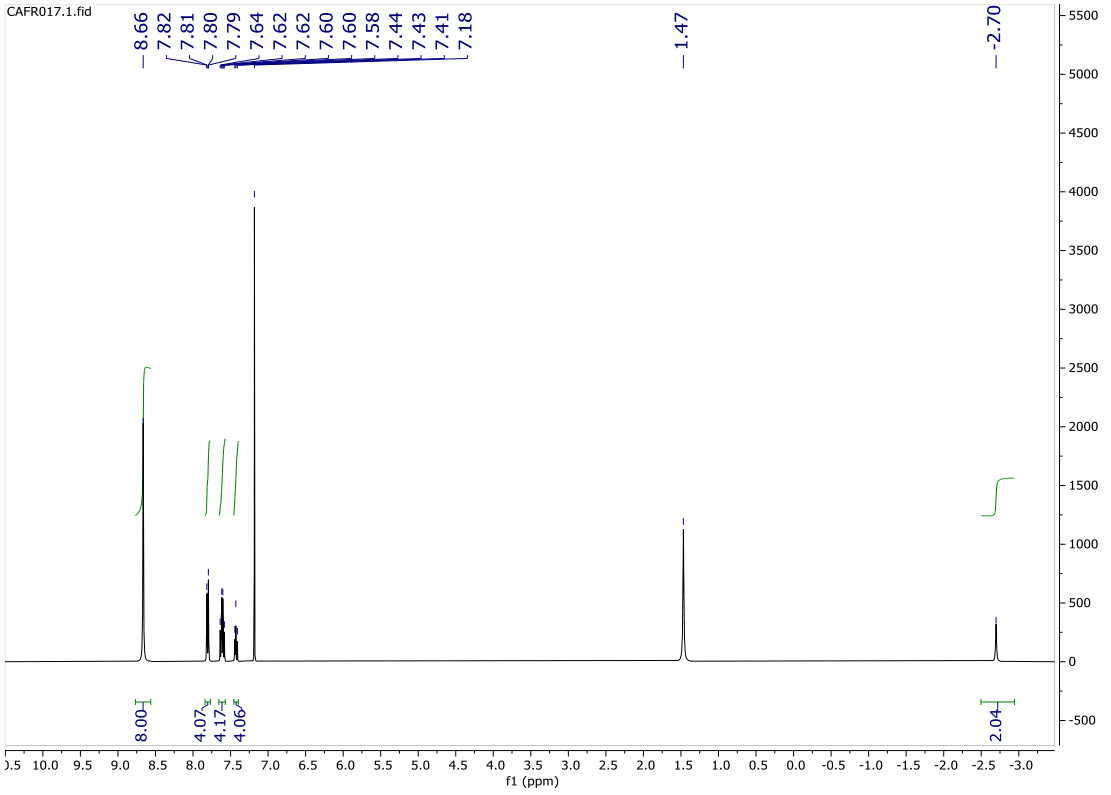

Figure S16: ^{1}H NMR in $CDCl_3$ of **3**

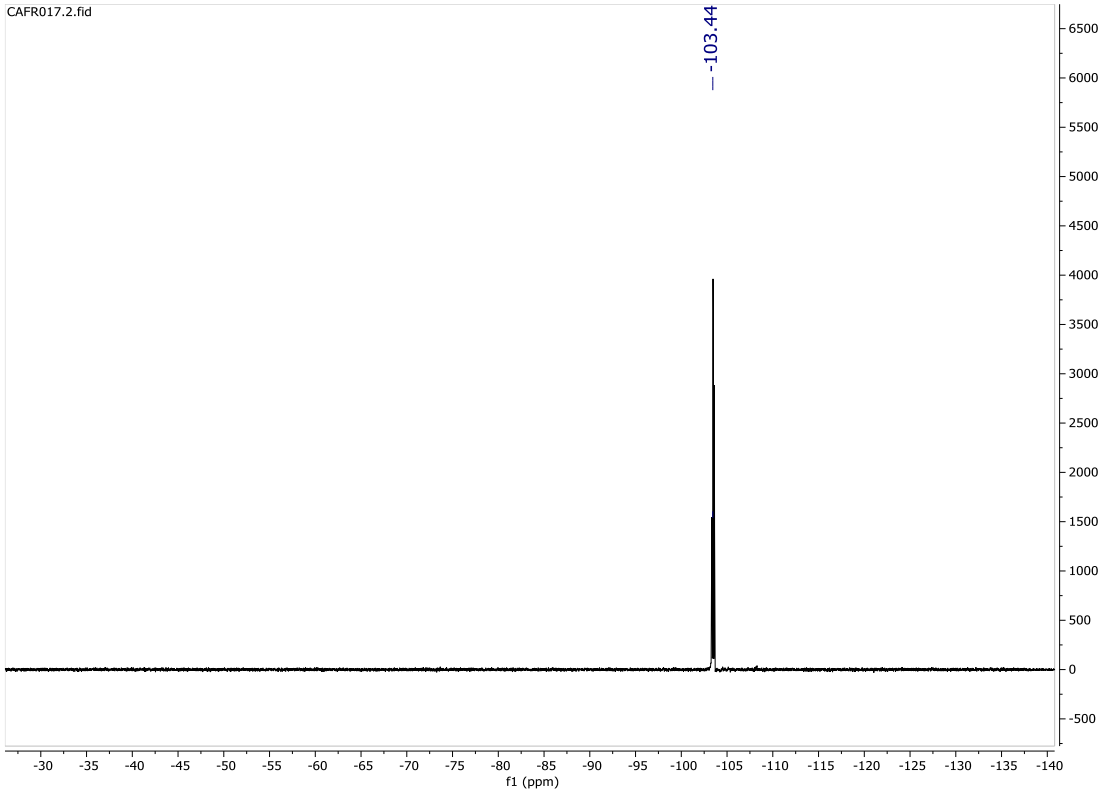

Figure S3: ^{19}F NMR in $CDCl_3$ of **3**

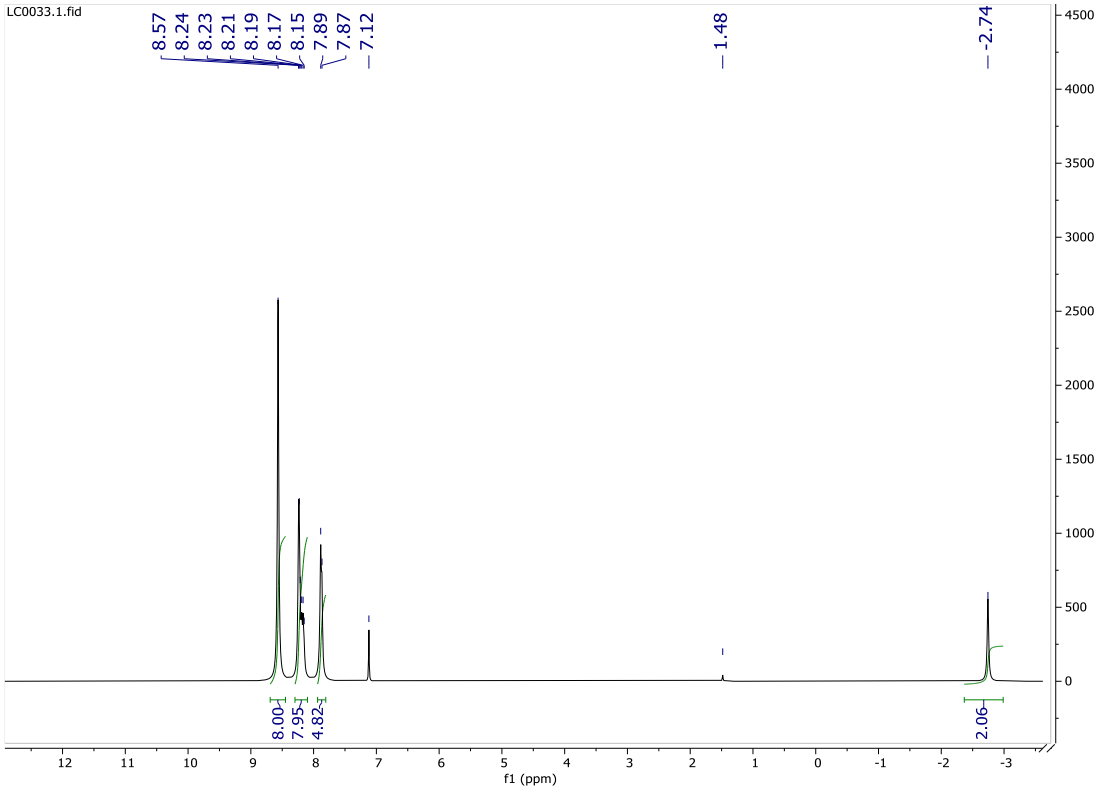

Figure S4: ^{1}H NMR in $CDCl_3$ of **4**

8.2 Iron porphyrins

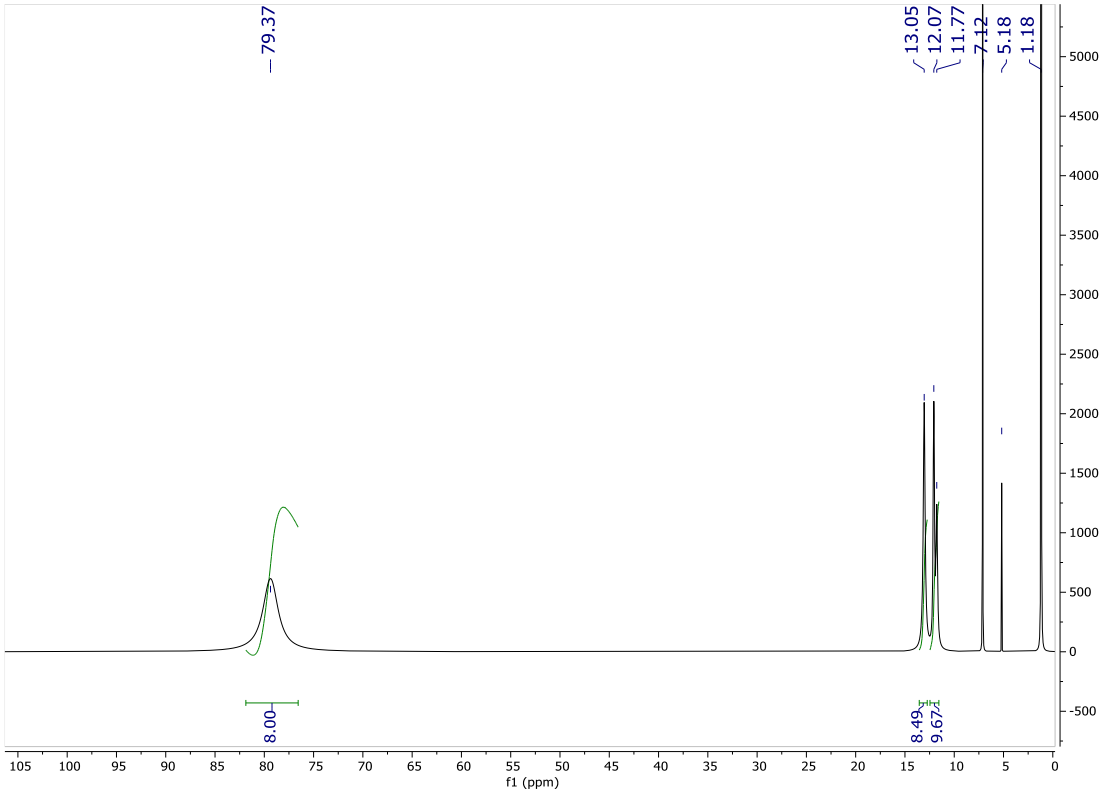

Figure S19: ^{1}H NMR in $CDCl_3$ of **1Fe**

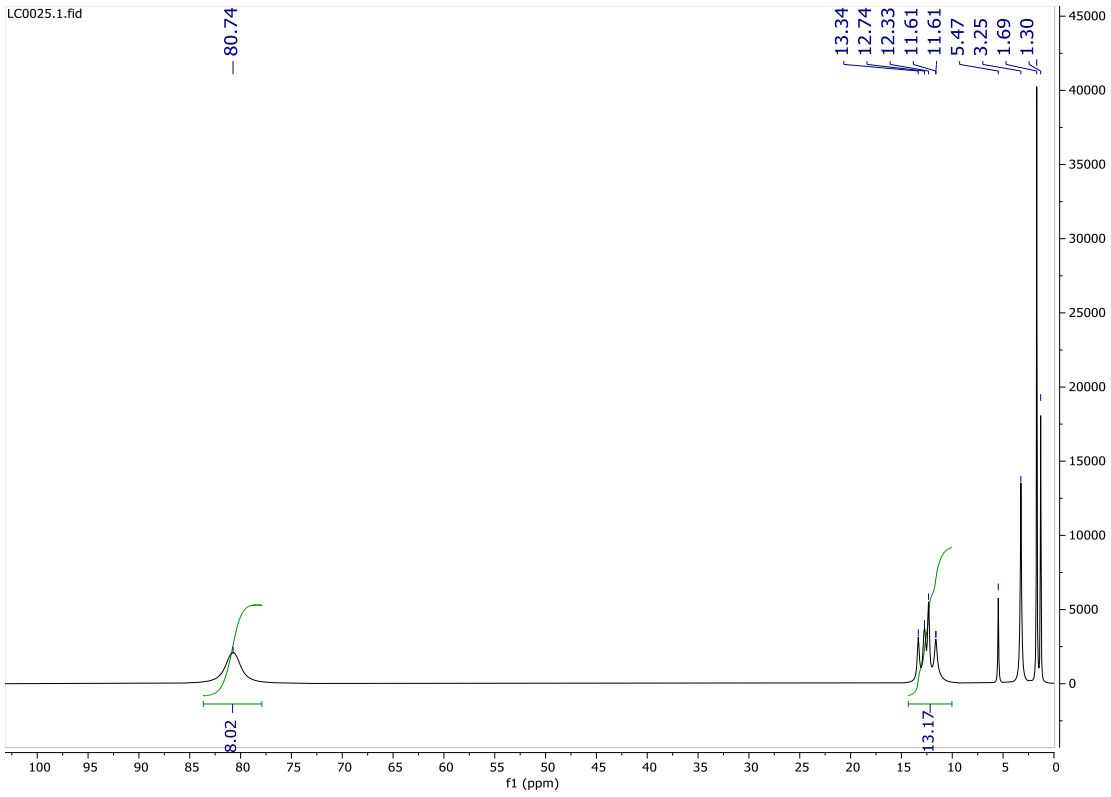

Figure S20: ^{1}H NMR in $CDCl_3$ of **2Fe**

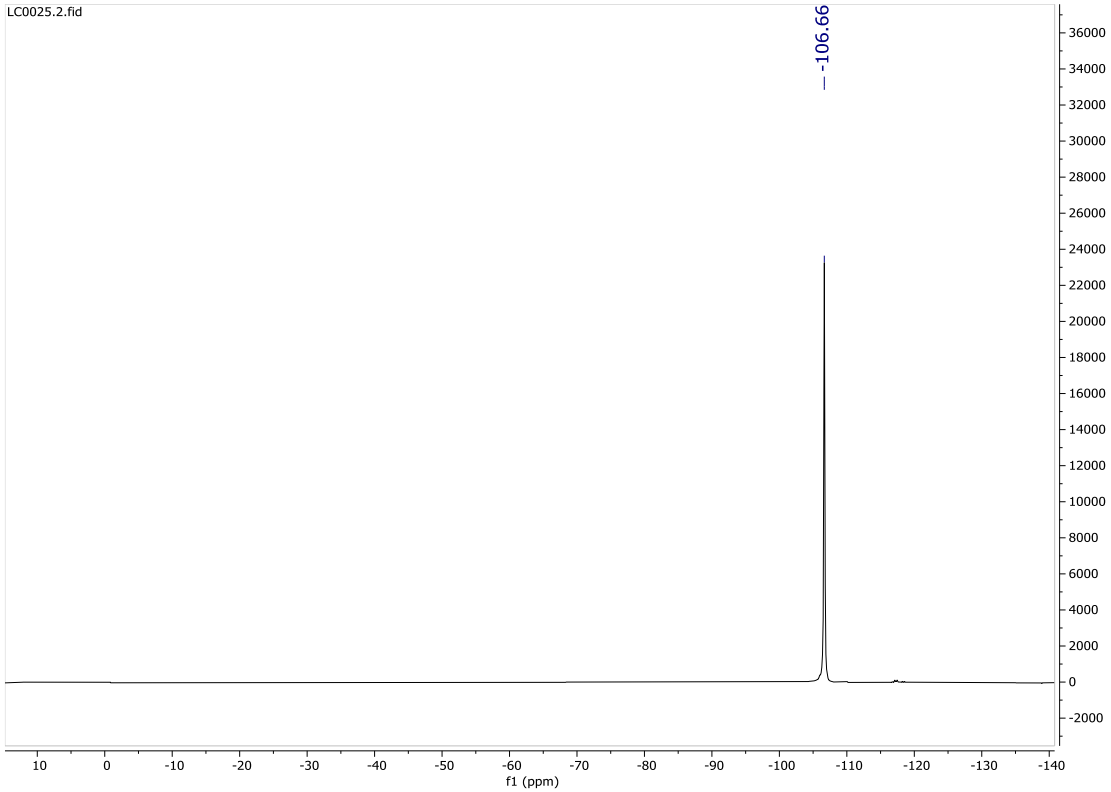

Figure S21: ^{19}F NMR in $CDCl_3$ of **2Fe**

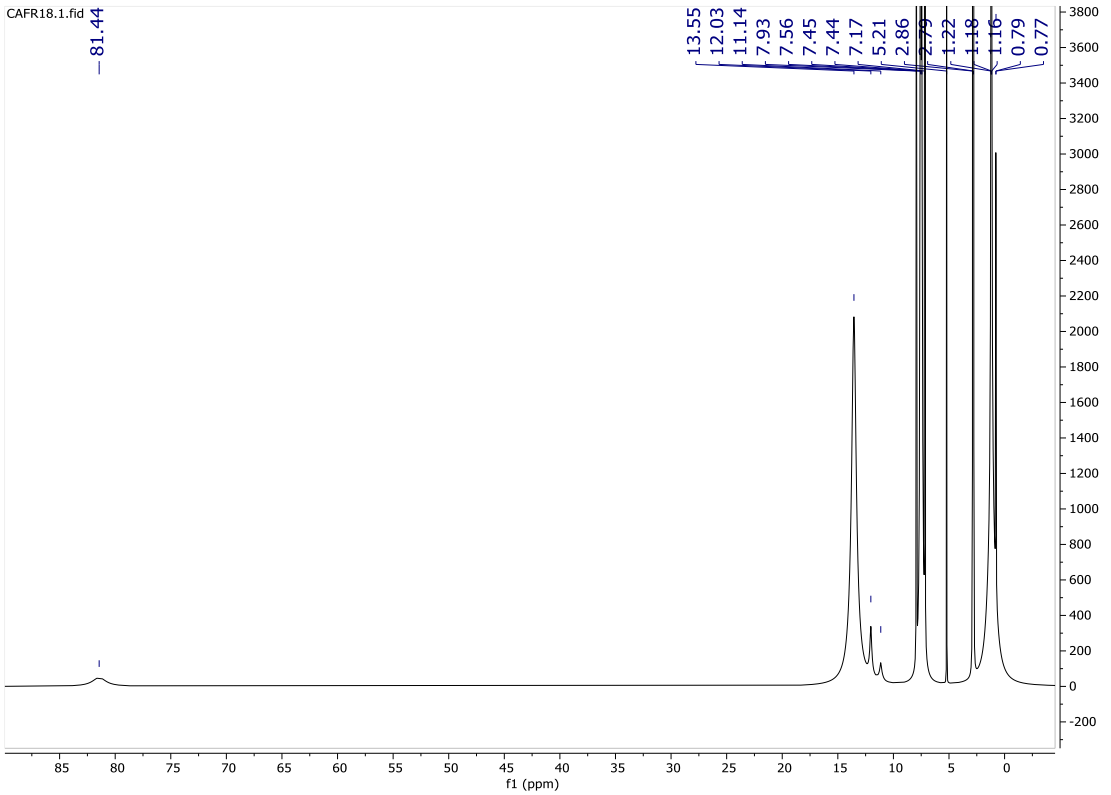

Figure S22: ^{1}H NMR in $CDCl_3$ of **3Fe**

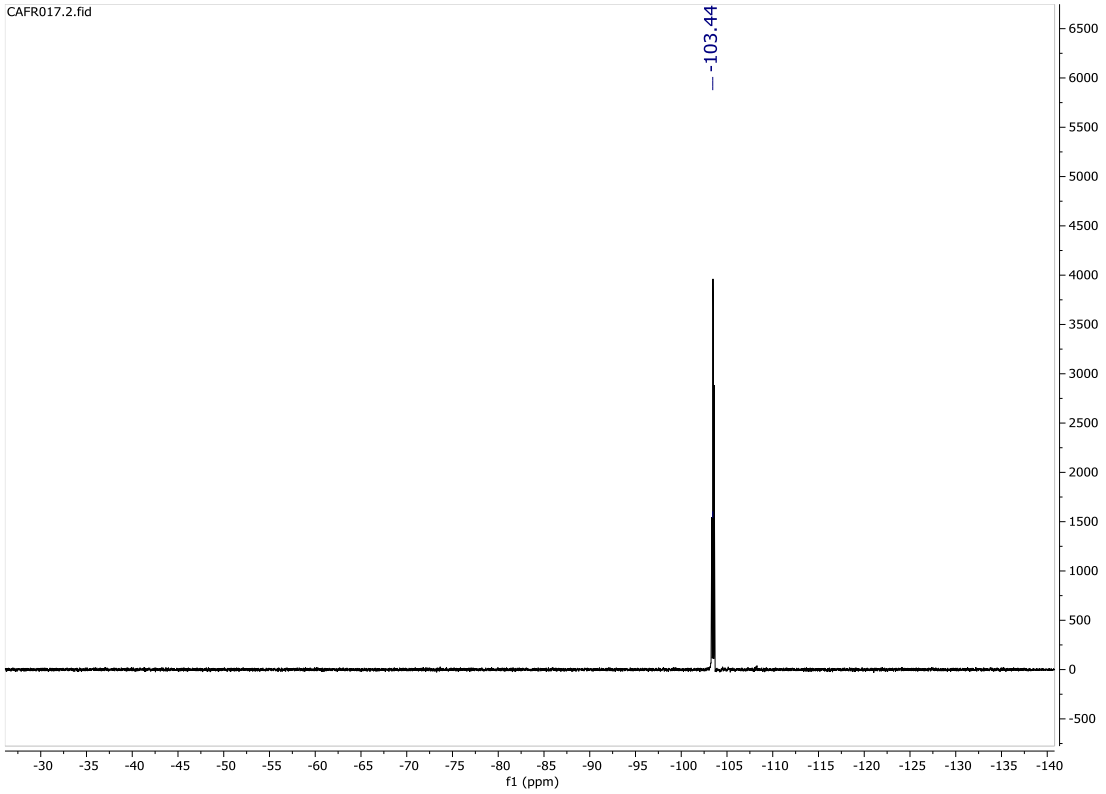

Figure S23: ^{19}F NMR in $CDCl_3$ of **3Fe**

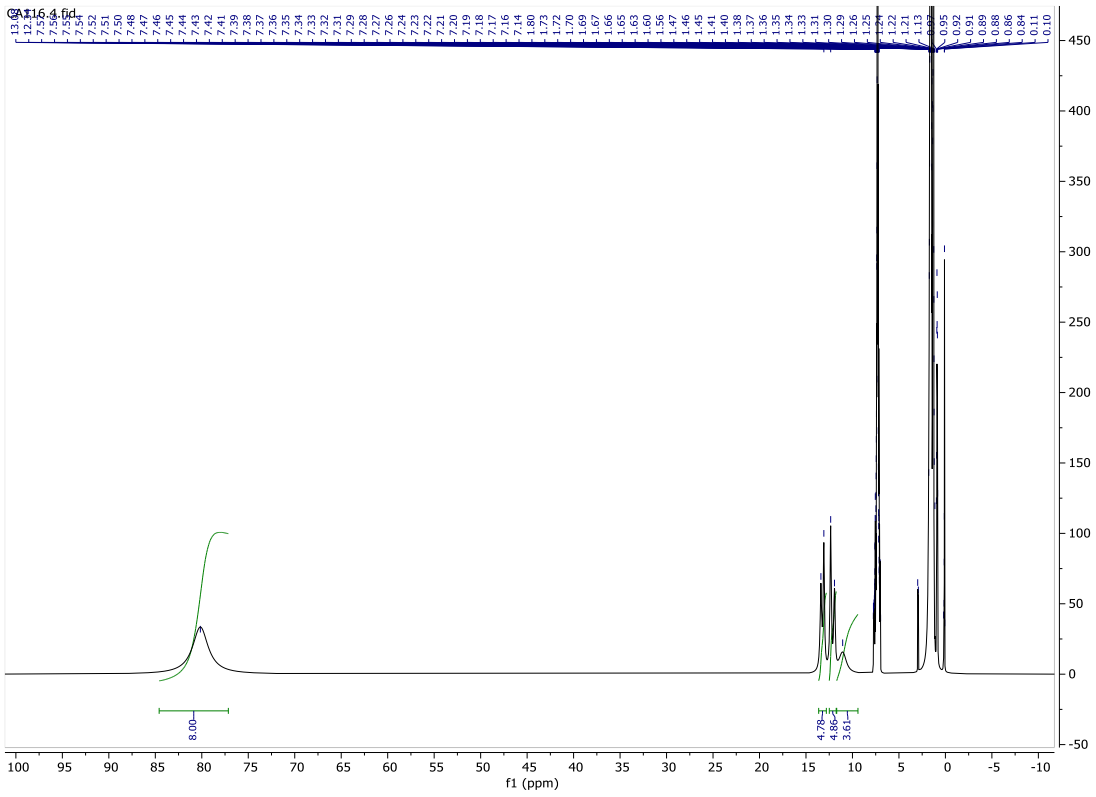

Figure S24: ^{1}H NMR in $CDCl_3$ of **4Fe**

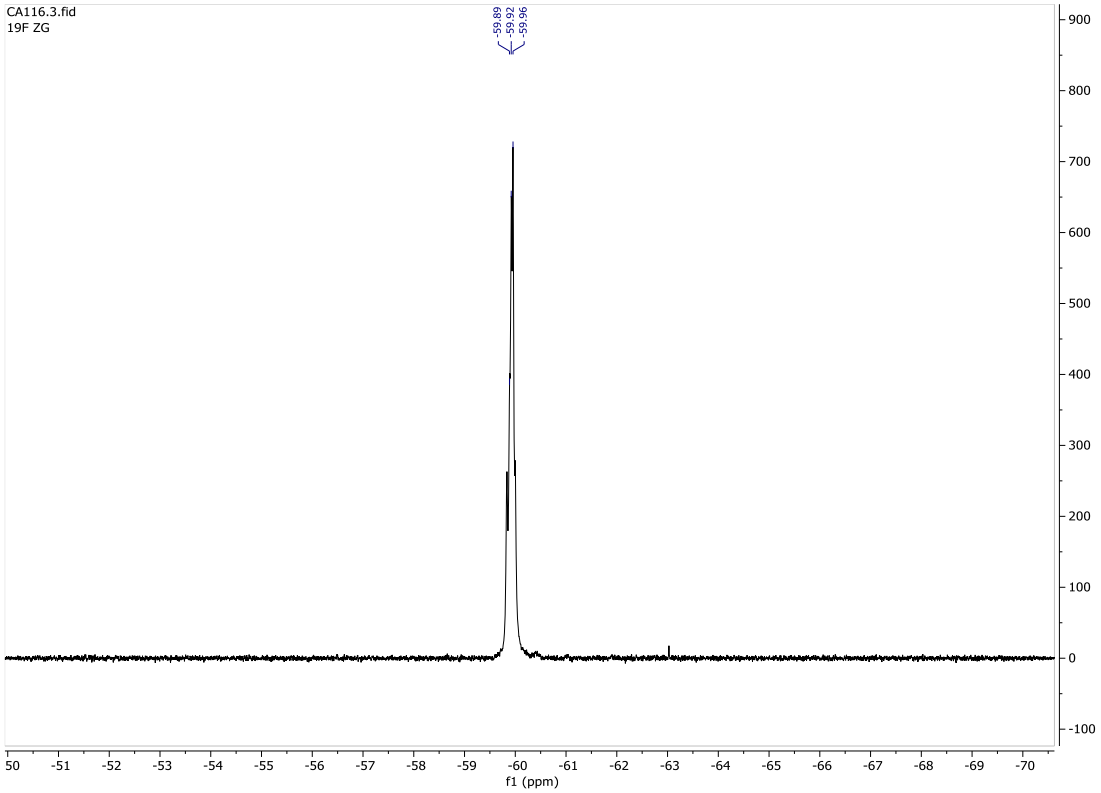

Figure S25: ^{19}F NMR in CDCl3 of **4Fe**

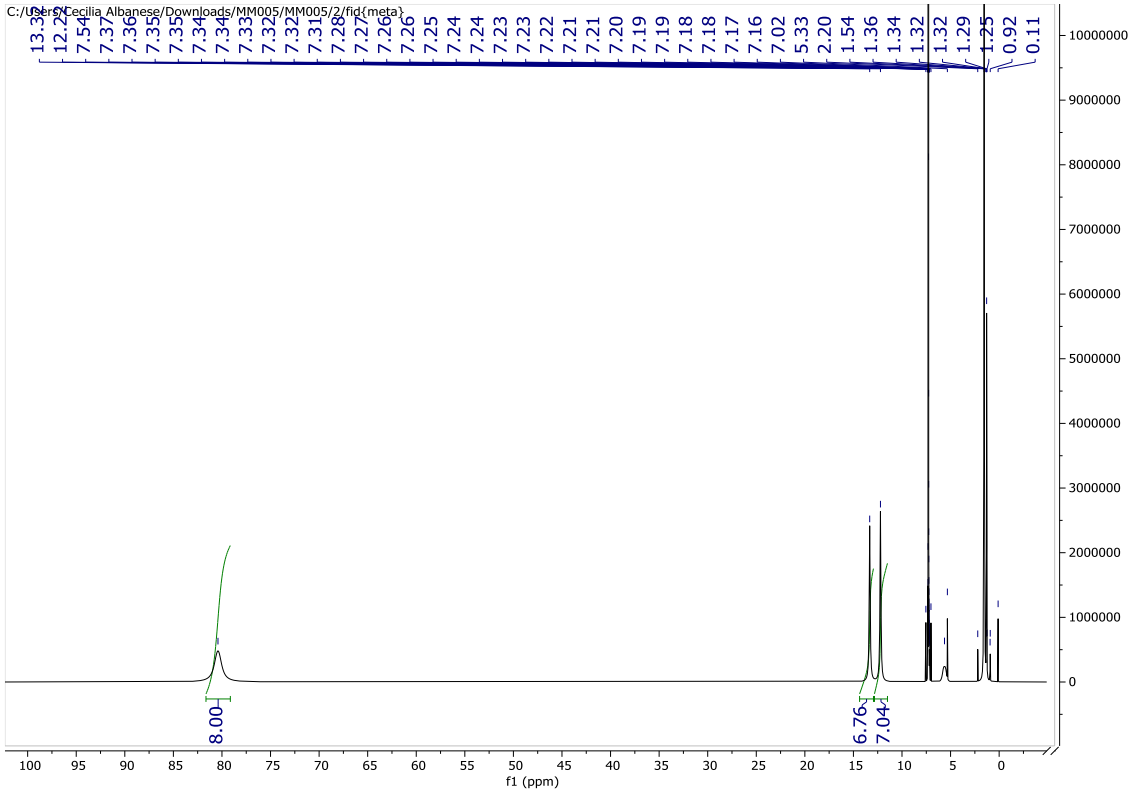

Figure S26: ^{1}H NMR in $CDCl_3$ of **5Fe**